The Development and Evolution of Two Atmospheric Rivers in Proximity to Western North Pacific Tropical Cyclones in October 2010

JASON M. CORDEIRA

Department of Atmospheric Science and Chemistry, Plymouth State University, Plymouth, New Hampshire

F. MARTIN RALPH

Physical Sciences Division, NOAA/Earth System Research Laboratory, Boulder, Colorado

BENJAMIN J. MOORE

Cooperative Institute for Research in Environmental Sciences, University of Colorado, Boulder, Colorado

(Manuscript received 15 January 2013, in final form 29 July 2013)

ABSTRACT

This study investigates the evolution of two zonally elongated atmospheric rivers (ARs) that produced >200 mm of rainfall over mountainous regions of Northern California in late October 2010. Synoptic-scale analysis and air parcel trajectory analysis indicate that the ARs developed within high-CAPE environments characterized by troposphere-deep ascent as water vapor was transported directly from western North Pacific tropical cyclones (TCs) toward the equatorward entrance region of an intensifying North Pacific jet stream (NPJ). The same ARs were subsequently maintained as water vapor was transported from extratropical and subtropical regions over the central and eastern North Pacific in an environment characterized by quasi-geostrophic forcing for ascent and strong frontogenesis along the anticyclonic shear side of an intense and zonally extended NPJ. Although the ARs developed in conjunction with water vapor transported from regions near TCs and in the presence of troposphere-deep ascent, an atmospheric water vapor budget illustrates that decreases in integrated water vapor (IWV) via precipitation are largely offset by the horizontal aggregation of water vapor along the AR corridors via IWV flux convergence in the presence of frontogenesis. The frameworks used for investigations of predecessor rain events ahead of TCs and of interactions between recurving TCs and the NPJ are also utilized to illustrate many dynamically similar processes related to AR development and evolution. Similarities include the following: water vapor transport directly from a TC, troposphere-deep ascent in a high-CAPE environment beneath the equatorward entrance region of an intensifying upper-tropospheric jet streak, interactions between diabatic outflow and an upper-tropospheric jet streak, and strong frontogenesis.

1. Introduction

A majority of extratropical water vapor transport in the atmosphere is focused within long (thousands of kilometers) and narrow (~500 km) regions of vertically integrated water vapor (IWV) that are frequently referred to as atmospheric rivers (ARs; Zhu and Newell 1998; Ralph et al. 2004; Neiman et al. 2008a,b, among others) or moisture conveyor belts (e.g., Bao et al. 2006; Knippertz and Martin 2007). The ARs are often found in the warm sector of transient maritime extratropical cyclones and can represent regions of concentrated IWV transport (IVT) along a precold-frontal low-level jet (e.g., Ralph et al. 2004) or regions of IVT into a narrow substructure of the broad ascending "warm conveyor belt" (e.g., Carlson 1980; Browning 1990; Carlson 1998; Eckhardt et al. 2004). The concentrated regions of IWV and IVT associated with ARs can also result in the transport of tropical water vapor into the extratropics (i.e., tropical moisture exports; Knippertz and Wernli 2010; Knippertz et al. 2013) or result in the lateral transport of subtropical and extratropical water vapor (e.g., Bao et al. 2006; Neiman et al. 2013). Once in the extratropics, Zhu and Newell (1998) indicate that IVT is

Corresponding author address: Jason M. Cordeira, Plymouth State University, 17 High St., MSC 48, Plymouth, NH 03264.
E-mail: j_cordeira@plymouth.edu

DOI: 10.1175/MWR-D-13-00019.1

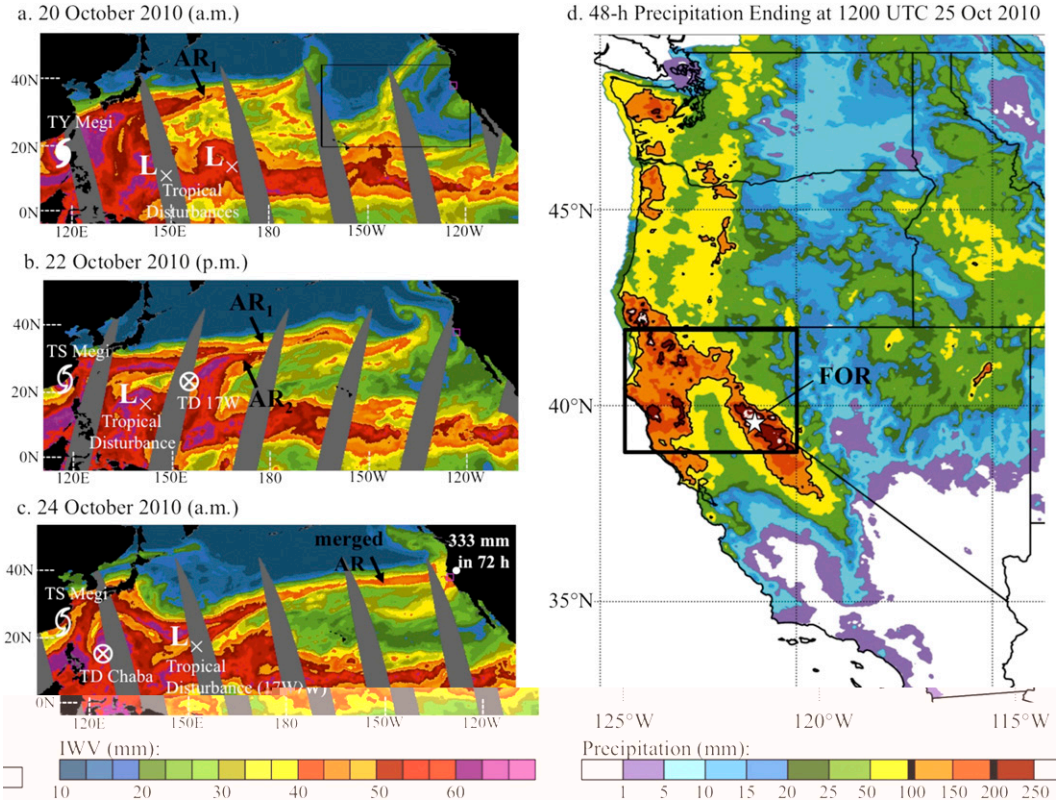

FIG. 1. Composite a.m. or p.m. SSM/I satellite measurements of integrated water vapor (mm; shaded according to scale) for two atmospheric rivers (''AR_1'' and ''AR_2'') at (a) 20, (b) 22, and (c) 24 Oct 2010. Locations of tropical cyclones over the western North Pacific are indicated by symbols and labeled. The SSM/I imagery is adapted from images provided by the NOAA/ESRL/Physical Sciences Division. (d) 48-h precipitation (mm; shaded according to scale and contoured at the 100- and 200-mm threshold) ending at 1200 UTC 25 Oct 2010. Precipitation data are analyzed from the NCEP National Stage-IV multisensor quantitative precipitation estimates. The location of the event maximum precipitation at Four Trees (FOR), CA, is labeled in (c) and (d). The black box in (d) denotes the climatological precipitation analysis domain discussed in section 1.

predominantly confined to ARs and that ~90% of the horizontal IVT occurs within only 10% of the hemispheric circumference.

The objective of the current study is to investigate the evolution of two zonally elongated ARs over the North Pacific basin in October 2010 (Figs. 1a–c). These two ARs developed in proximity to three tropical cyclones (TCs) (TCs Megi, Chaba, and 17W) in the western and central North Pacific and contained contiguous regions of high IWV values as they crossed the North Pacific between 20 and 24 October 2010. The two ARs in this study ultimately merged over the central and eastern North Pacific and made landfall over Northern California on 24 October 2010. The landfall of the merged AR was associated with 48-h precipitation totals >200 mm ending at 1200 UTC 25 October 2010 (Fig. 1d) over coastal and interior mountainous regions of Northern California. The locations of the highest precipitation totals are consistent with orographic enhanced precipitation commonly associated with landfalling ARs (e.g., Ralph et al. 2003, 2004, 2005, 2006; Neiman et al. 2008a,b, 2011; Stohl et al. 2008; Smith et al. 2010; Ralph and Dettinger 2012). The highest event total precipitation was 333 mm at Four Trees (FOR), California (elevation of 1450 m MSL), for the 72-h period ending at 1200 UTC 25 October 2010. This precipitation total indicates that the event was classified as an ''R-Cat 2'' case using the extreme event scaling criteria from Ralph and Dettinger (2012). A climatological analysis of 48-h area-averaged precipitation totals over Northern California (i.e., over the region encompassed by the black box in Fig. 1d) indicates that the landfall of the merged AR was associated with the largest 48-h October precipitation event between 1970 and 2010.

The development of the two ARs in this study in proximity to TCs Megi, Chaba, and 17W, and subsequent landfall of the merged AR over Northern California suggests that western North Pacific TCs may influence the

occurrence of autumnal extreme precipitation events in association with landfalling ARs along the west coast of North America. This study is applicable to another strong, zonally oriented AR that impacted California in October 2009 (Ralph and Dettinger 2011), which also produced R-Cat 2 magnitude precipitation. A majority of observational and numerical modeling studies to date demonstrate that western North Pacific TCs can influence sensible weather far downstream via the evolution of the large-scale flow. These studies emphasize the interaction between a TC and the extratropical waveguide during recurvature and extratropical transition that can result in a significant large-scale flow response in association with Rossby wave train amplification and dispersion (e.g., Harr and Elsberry 2000; Klein et al. 2002; Atallah and Bosart 2003; McTaggart-Cowan et al. 2007a,b; Riemer et al. 2008; Harr and Dea 2009; Riemer and Jones 2010; Archambault 2011; Archambault et al. 2013). Recent studies have also demonstrated that a TC can influence extreme precipitation events in the form of predecessor rain events (PREs) far downstream of TCs in association with water vapor transport over large horizontal distances.

The present study explores whether the physical processes that contribute to the development of an AR in proximity to a TC is similar to the physical processes that contribute to the development of PREs and whether or not the extreme precipitation event over Northern California can be considered a PRE. PREs are a type of extreme precipitation event that occur in conjunction with water vapor transport far downstream of a TC (Cote 2007; Galarneau et al. 2010). These mesoscale rainstorms are associated with rainfall rates $\geq 100\,\mathrm{mm\,day^{-1}}$ and typically occur ~1000 km downstream of TCs. Composite analyses and case studies of PREs over the United States indicate that PREs develop when a broad plume of atmospheric precipitable water (i.e., IWV) emanating from a TC along a low-let jet intersects a quasi-stationary baroclinic zone and is forced to ascend in conjunction with a thermally direct lower-tropospheric frontogenetic circulation in the equatorward entrance region of a quasi-stationary and intensifying upper-tropospheric jet streak (Bosart and Carr 1978; Bosart and Dean 1991; Cote 2007; Galarneau et al. 2010; Moore 2010; Schumacher et al. 2011; Bosart et al. 2012; Moore et al. 2013). Although much of the research on PREs has been focused on events over the United States, PREs have also been shown to occur over eastern Asia ahead of western North Pacific TCs (e.g., Wang et al. 2009; Byun and Lee 2012).

Comparisons among past studies of ARs, including studies of moisture conveyor belts and tropical moisture exports, and PREs suggest that the horizontal transport of water vapor from TCs represent a form of tropical moisture export that could lead to AR formation [e.g., see Figs. 3 and 6 of Stohl et al. (2008) and Figs. 7a,b of Knippertz et al. (2013)]. The formation of such an AR, however, would need to overcome the potential deleterious effect of atmospheric IWV removal via precipitation processes in the presence of saturated, troposphere-deep upright ascent in the case of a PRE or sloped air parcel ascent in the case of a warm conveyor belt. Given the longevity of such an AR if it were to subsequently cross the North Pacific, we hypothesize that the deleterious effect of precipitation on the IWV tendency within these ARs is likely offset by water vapor flux convergence within regions of frontogenesis in the AR region as suggested by Bao et al. (2006) and Neiman et al. (2013). The proposed hypothesis for the formation and evolution of the two zonally elongated ARs in the present study is explored via traditional synoptic-scale analyses, an AR water vapor budget, and a Lagrangian trajectory analysis.

2. Data sources and methodologies

Special Sensor Microwave Imager (SSM/I) satellite measurements (Hollinger 1991), obtained from the National Oceanic and Atmospheric Administration Earth System Research Laboratory (NOAA/ESRL) Physical Sciences Division, and the National Centers for Environmental Prediction (NCEP) National Stage-IV multisensor quantitative precipitation estimates (Baldwin and Mitchell 1997) on a 4-km grid were shown in Fig. 1. The Climate Prediction Center (CPC) unified precipitation dataset (UPD) was used to quantify 48-h area-averaged historical precipitation over Northern California discussed in section 1. The remainder of the study utilizes the NCEP Climate Forecast System Reanalysis (CFSR; Saha et al. 2010). The NCEP CFSR was obtained on a ~0.5° latitude × ~0.5° longitude grid with 37 isobaric levels (1000–1 hPa) and 6-h temporal resolution.

We adopt a methodology similar to investigations of PREs by Galarneau et al. (2010) and diagnose AR evolution within the quasigeostrophic (QG) and potential vorticity (PV) frameworks. Within these frameworks, regions of QG forcing for ascent are diagnosed with the right-hand side of the **Q**-vector form of the QG omega equation (Hoskins et al. 1978). The **Q**-vector form of the QG omega equation is evaluated at 700 hPa, neglecting the beta term, as in Bluestein [1992, Eq. (5.7.56)] as

$$-\frac{1}{2}\left(\nabla_p^2+\frac{f_0^2}{\sigma}\frac{\partial^2}{\partial p^2}\right)\omega=\nabla_p\cdot\mathbf{Q}, \tag{1}$$

where **Q** is defined as in Bluestein [1992, Eq. (5.7.55)] as

$$\mathbf{Q} = -\frac{R}{\sigma p}\begin{pmatrix} \frac{\partial \mathbf{V}_g}{\partial x}\cdot\nabla_p T \\ \frac{\partial \mathbf{V}_g}{\partial y}\cdot\nabla_p T \end{pmatrix} = \begin{pmatrix} Q_1 \\ Q_2 \end{pmatrix}. \quad (2)$$

The variables in these equations have their usual meteorological meanings. Regions of **Q**-vector convergence (divergence) from Eq. (2) are indicative of regions of QG forcing for ascent (descent) at 700 hPa.

The QG framework is complemented by investigation of environmental parameters conducive to troposphere-deep convection such as large values of convective available potential energy (CAPE) and midtropospheric upward vertical motion. The corresponding upper-tropospheric diabatic outflow associated with troposphere-deep convection is illustrated via the irrotational component of the horizontal wind near the level of the tropopause at 250 hPa. The PV framework is subsequently utilized to assess the influence of troposphere-deep convection and upper-tropospheric outflow on the tropopause-level distribution of PV in the vicinity of the jet stream as used in studies on the extratropical flow response to recurving western North Pacific TCs (e.g., Archambault et al. 2013).

Horizontal frontogenesis is computed at 700 hPa as two-dimensional scalar frontogenesis following the form of Miller (1948), and is defined as the Lagrangian rate of change in the magnitude and direction of the horizontal potential temperature gradient vector. The horizontal frontogenesis F is defined mathematically as

$$F = \frac{d}{dt}|\nabla\theta| = \frac{\partial}{\partial t}|\nabla\theta| + \mathbf{V}_h\cdot\nabla|\nabla\theta|, \quad (3)$$

and is computed from the General Meteorological Package (GEMPAK; Koch et al. 1983) frontogenesis function following the notation of Keyser et al. (1988) as

$$F = \frac{d}{dt}|\nabla\theta| = -\frac{1}{2}|\nabla\theta|[D - E\cos(2\beta)], \quad (4)$$

which includes horizontal divergence D, resultant deformation E, and the orientations of axes of dilatation to the potential temperature contours (encompassed in β).

The general form of the atmospheric water vapor budget (e.g., Schmitz and Mullen 1996; Trenberth and Guillemot 1996) is used to estimate[1] the relative contributions of IVT divergence, evaporation, and precipitation to the time tendency in IWV as

$$\frac{\partial[\mathrm{IWV}]}{\partial t} = -\nabla\cdot\mathrm{IVT} + E - P, \quad (5)$$

where E is evaporation rate from the surface and P is the precipitation rate. The evaporation rate from the surface is obtained by multiplying the NCEP CFSR surface latent heat flux by the latent heat of vaporization, $L_v = 2.5\times10^6\,\mathrm{J\,kg^{-1}}$, and the precipitation rate is obtained from the rainfall rate in the National Aeronautics and Space Administration's (NASA's) Tropical Rainfall Measuring Mission (TRMM) dataset (Huffman et al. 2007). The IVT is calculated similar to the methodologies of Neiman et al. (2008b) and Moore et al. (2012) from the NCEP CFSR as

$$\mathrm{IVT} = -\frac{1}{g}\int_{p_b}^{p_t}(q\mathbf{V}_h)\,dp, \quad (6)$$

where q is the specific humidity, $\mathbf{V}_h$ is the horizontal wind vector, p_b is 1000 hPa, p_t is 200 hPa, and g is the acceleration due to gravity. Finally, "single layer" contributions to the IVT (hereafter referred to as the "partial IVT") are shown in cross sections as

$$\text{partial IVT} = -\frac{1}{g}\int_{p_1}^{p_2}(q\mathbf{V}_h)\,dp, \quad (7)$$

where p_1 and p_2 indicates two consecutive isobaric levels.

3. AR evolution

A 6-day time-mean analysis of IVT magnitude and direction illustrates several apparent water vapor source regions and water vapor transport pathways for 19–24 October 2010 during the life cycles of the two ARs over the North Pacific (Fig. 2). These regions of time-mean IVT are located to the northeast and northwest of TCs Megi and Chaba, respectively, to the northeast of 17W, and equatorward of the time-mean zonally extended North Pacific jet stream (NPJ) over the eastern North Pacific. These regions of time-mean IVT represent water vapor transport associated with the first AR (i.e., AR_1), the second AR (i.e., AR_2), and the merged AR, respectively.

Daily analyses of IWV (Figs. 3a–e) and IVT (Figs. 3f–j) illustrate that water vapor is initially transported from locations near TCs Megi and Chaba to a location within the equatorward entrance region of the NPJ on 20 October 2010 (Figs. 3a,f). The development of AR_1 is defined as the formation of a corridor of IWV values >40 mm and

[1] We can only estimate the relative contributions to the total atmospheric water vapor budget given that the terms on the right-hand side of Eq. (5) are derived from mixed datasets.

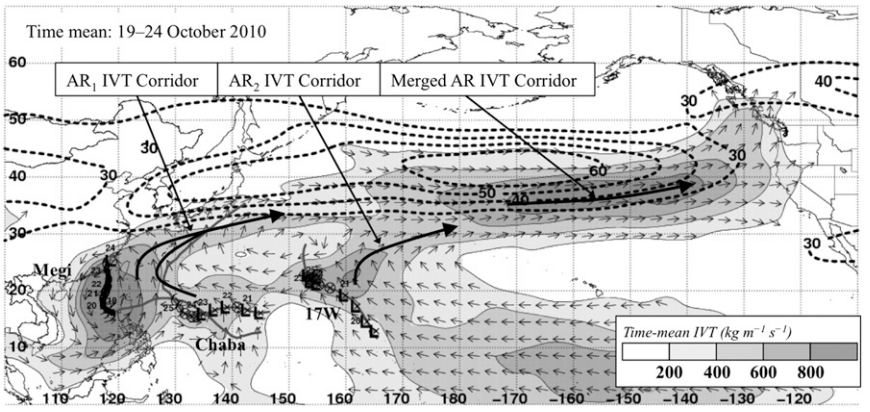

FIG. 2. The 19–24 Oct 2010 time-mean 250-hPa wind speed ($m\,s^{-1}$; dashed contours) and vertically integrated water vapor transport ($kg\,m^{-1}\,s^{-1}$; thin solid contours and shaded with vectors denoting transport direction). The tracks of TCs Megi, Chaba, and 17W are drawn in gray for the total duration of each cyclone. The TC locations are indicated by symbols according to the key at 0000 and 1200 UTC between 19 and 24 Oct 2010. Day of month (October) is indicated at 0000 UTC near each TC location. The data source is the NCEP CFSR.

IVT magnitude values $>400\,kg\,m^{-1}\,s^{-1}$ that extends poleward from the tropical IWV reservoir of TCs Megi and Chaba.[2] The development of AR_1 occurs between 1200 UTC 20 October and 1200 UTC 21 October 2010 as the length of the corridor of IWV (>3000 km) increases relative to its width (~500 km; Figs. 3a,b,f,g). The AR_1 contains IWV values >50 mm and IVT values $>500\,kg\,m^{-1}\,s^{-1}$, and is located in the equatorward entrance region of the NPJ ($>80\,m\,s^{-1}$) at 1200 UTC 21 October 2010 (Figs. 3b,f). At the same time, a frontal low pressure system develops at the eastern edge of AR_1 in the equatorward entrance region of the NPJ over the western North Pacific (Fig. 3b).

The development of AR_2 is similarly defined as the formation of a corridor of IWV values >40 mm and IVT magnitude vales $>400\,kg\,m^{-1}\,s^{-1}$ that extends poleward from the tropical IWV reservoir associated with TC 17W. The development of AR_2 occurs at ~1200 UTC 22 October 2010 as the length of the corridor of IWV (>3000 km) increases relative to its width (~500 km; Figs. 3c,h). The AR_1 leads AR_2 by ~2000 km and their associated regions of IWV and IVT merge into a single AR (hereafter referred to as the ''merged AR'') along the anticyclonic shear side of an intensifying NPJ ($>90\,m\,s^{-1}$) by 1200 UTC 23 October 2010 (Figs. 3d,i). Water vapor associated with the merged AR is subsequently transported to the east across the North Pacific toward western North America on 23 and 24 October 2010 within the equatorward exit region of the NPJ (Figs. 3d,e,i,j). The maximum IVT magnitude associated with the merged AR during this period is $>1000\,kg\,m^{-1}\,s^{-1}$ in association with IWV values of 40–50 mm and a vertically averaged mean horizontal wind speeds $>20\,m\,s^{-1}$ (not shown). The IVT magnitudes $>1000\,kg\,m^{-1}\,s^{-1}$ are larger than the maximum IVT magnitudes of ~1000 and $\sim650\,kg\,m^{-1}\,s^{-1}$ found in recent case studies of strong landfalling ARs over the eastern North Pacific by Neiman et al. (2008b) and Ralph et al. (2011), respectively. This difference in IVT magnitude is likely attributable to the large vertically averaged mean horizontal wind speeds as the AR becomes coupled with the intensifying $90\,m\,s^{-1}$ NPJ (subsequently discussed in association with Fig. 4).

The frontal low pressure system at the eastern edge of AR_1 propagates rapidly eastward at a speed $>25\,m\,s^{-1}$ and deepens from a sea level pressure of ~996 hPa on 22 October 2010 to <964 hPa on 24 October 2010 (Figs. 3c–e). Additional analysis (not shown) of the rapidly deepening frontal low pressure system indicates that the cyclone contains characteristics similar to case studies of diabatic Rossby waves and their role in rapid cyclone intensification (e.g., Wernli et al. 2002; Moore et al. 2008; Cordeira and Bosart 2011). These characteristics are further discussed in section 6.

The development of AR_1 occurred in conjunction with an increase in the magnitude of the partial IVT from ~100 to $>125\,kg\,m^{-1}\,s^{-1}$, an increase in the depth of the AR (e.g., an increase in the altitude of the 50 and $75\,kg\,m^{-1}\,s^{-1}$ partial IVT magnitude contours), and an

[2] These IWV and IVT magnitude values represent the ~75th percentile of all gridpoint values over the North Pacific basin (20°–50°N, 120°E–120°W) during 20–24 October 2010. The AR definition includes an IVT threshold, which is in contrast to previous studies, which have used IWV thresholds and AR structure in their definitions (e.g., IWV > 20 mm, length > 2000 km, and width < 1000 km; see Neiman et al. 2008b).

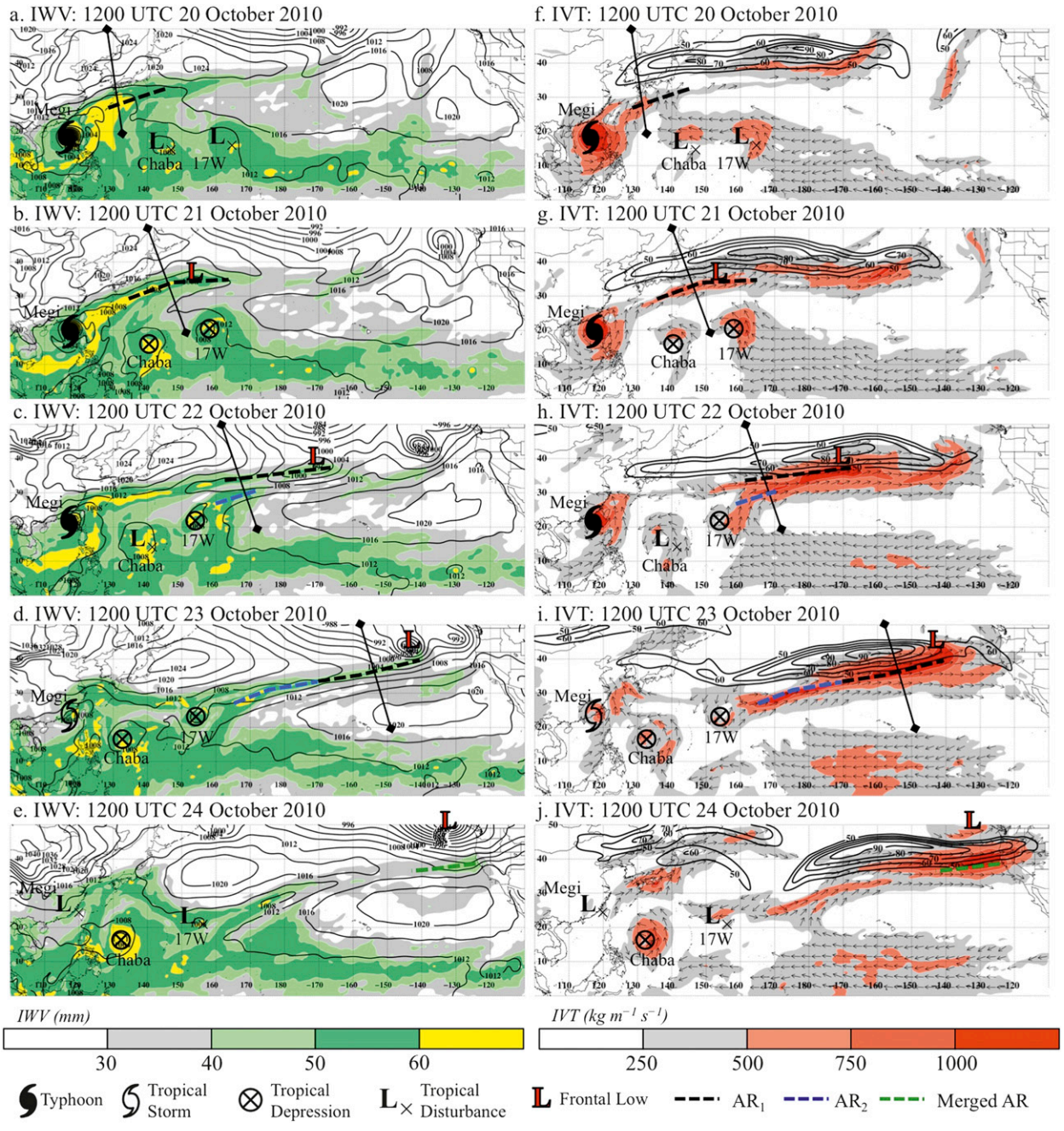

FIG. 3. (a)–(e) IWV (mm; shaded) and sea level pressure (hPa; solid contours) at 1200 UTC on 20–24 Oct 2010. (f)–(j) IVT magnitude ($kg\,m^{-1}\,s^{-1}$; shaded), IVT direction (constant length vectors), and 250-hPa wind speed (contours every $10\,m\,s^{-1}$ beginning at $50\,m\,s^{-1}$) at 1200 UTC on 19–24 Oct 2010. The locations of TC Megi, Chaba, and 17W, and a frontal low pressure system are indicated by symbols according to the key. The locations of AR_1, AR_2, and the merged AR are indicated by dashed, colored lines. Barbell lines pertain to cross-sectional analyses in Figs. 4 and 7. The data source is the NCEP CFSR.

increase in the magnitude of the NPJ from 60 to $>70\,m\,s^{-1}$ between 1200 UTC 20 October (Fig. 4a) and 1200 UTC 21 October (Figs. 4b). The subsequent evolution of AR_1 occurs in conjunction with an increase in the cross-sectional area encompassed by partial IVT magnitudes $>125\,kg\,m^{-1}\,s^{-1}$, an increase in the depth of the AR, and an increase in the area encompassed by upper-tropospheric wind speed values $>70\,m\,s^{-1}$ within the NPJ between 1200 UTC 21 October and 1200 UTC 22 October 2010 (Figs. 4b,c).

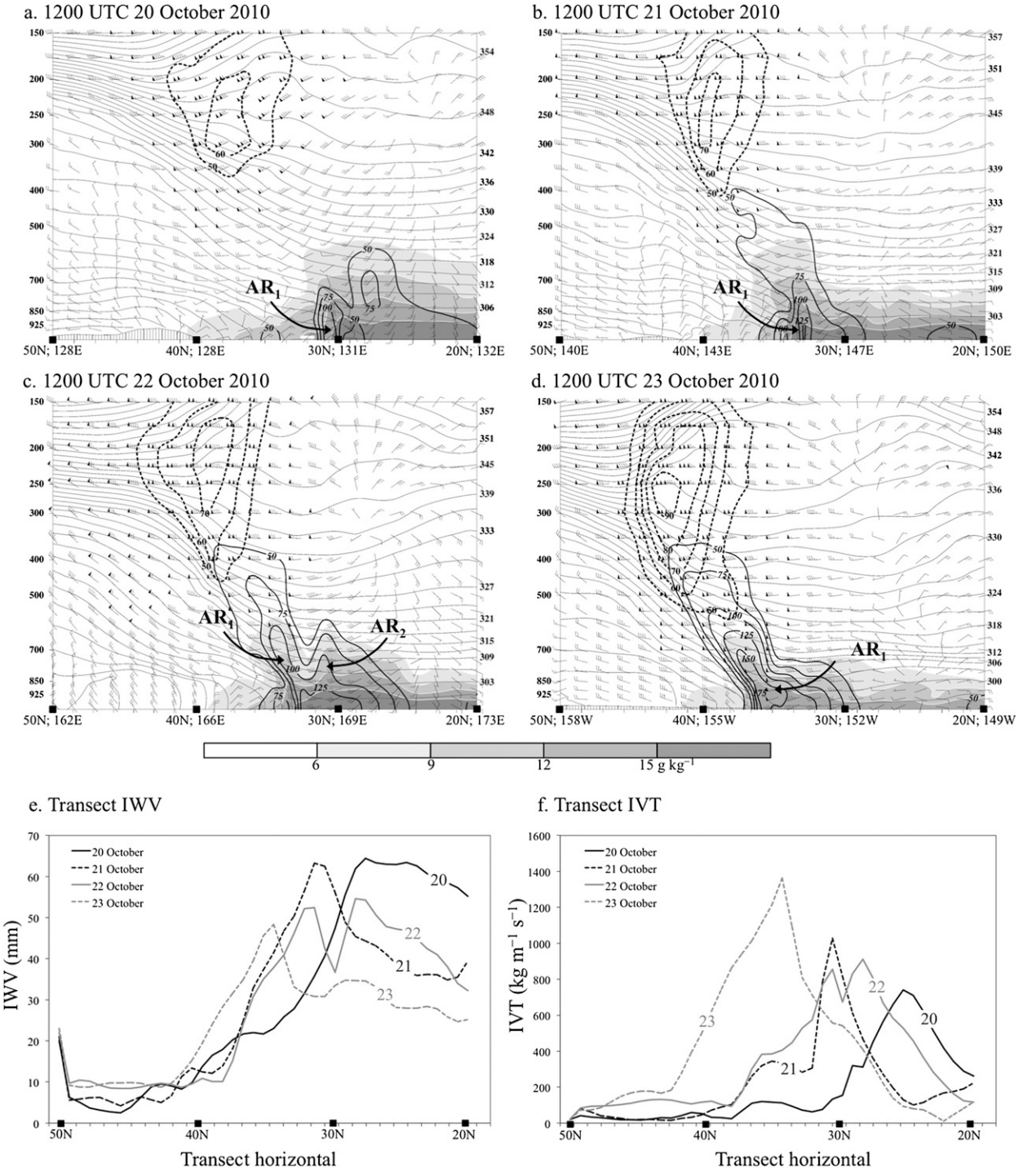

FIG. 4. Cross sections of horizontal wind speed (dashed contours every $10\,m\,s^{-1}$ beginning at $50\,m\,s^{-1}$), horizontal wind (pennant = $25\,m\,s^{-1}$, long barb = $5\,m\,s^{-1}$, and short barb = $2.5\,m\,s^{-1}$), potential temperature (K; solid gray contours labeled along right vertical axis), water vapor mixing ratio ($g\,kg^{-1}$; shaded), and horizontal water vapor transport (solid contours every $25\,kg\,m^{-1}\,s^{-1}$ beginning at $25\,kg\,m^{-1}\,s^{-1}$) at 1200 UTC on (a)–(d) 20–23 Oct 2010. Transect (e) IWV (mm) and (f) IVT ($kg\,m^{-1}\,s^{-1}$) at 1200 UTC on 20–23 Oct 2010 are provided. Horizontal cross-sectional lines are provided in Figs. 3, 5, and 6. Pressure is labeled along left vertical axis in hPa. The data source is the NCEP CFSR.

The AR_2 is also initially characterized by lower-tropospheric water vapor mixing ratio values $>15\,g\,kg^{-1}$ and partial IVT magnitudes $>125\,kg\,m^{-1}\,s^{-1}$ at 1200 UTC 22 October 2010 (Fig. 4c). The development and evolution of AR_2, including the subsequent merger of AR_1 and AR_2, occurred in conjunction with an amalgamation of the lower-tropospheric water vapor mixing ratio fields and partial IVT fields and an increase in the depth of the merged AR to ~550 hPa as determined by the altitude of the $100\,kg\,m^{-1}\,s^{-1}$ partial IVT magnitude contour during 22–23 October 2010 (Figs. 4c,d). The increase in the depth of the merged AR is primarily associated with an increase in the magnitude of the midtropospheric horizontal wind and a lowering corridor of maximum wind associated with the NPJ (Figs. 4c,d).

The water vapor mixing ratio and partial IVT associated with AR_1 is initially vertically oriented on 20 and 21 October 2010 (Figs. 4a,b) and gradually becomes tilted poleward with height in the equatorward entrance region of the NPJ by 22 and 23 October 2010 (Figs. 4c,d). Similarly, the water vapor mixing ratio and partial IVT associated with AR_2 is tilted in the vertical on 22 October 2010 (Fig. 4c) and is tilted poleward with height on 23 October 2010 (not shown). The change in the vertical orientation of the water vapor mixing ratio and partial IVT occurs in association with a decrease in the transect-relative IWV (Fig. 4e) and an increase in the magnitude of the transect-relative IVT (Fig. 4f). The temporal evolution of the vertical orientation of the ARs and the transect-relative IWV and IVT values suggest a tropical to extratropical transition in the environment containing the ARs as they become ''coupled'' to the thermally direct ageostrophic circulation in the entrance region of the NPJ.

4. Environmental evolution

a. Horizontal perspective

The AR_1 and AR_2 develop in association with a meridional contraction and zonal extension of high IWV values >50 mm in the equatorward entrance region of a quasi-stationary and intensifying NPJ (Fig. 5; also cf. Fig. 3). Both ARs form in environments characterized by troposphere-deep ascent illustrated by regions of 600-hPa upward vertical motion with a magnitude that exceeds $-9\times10^{-3}\,hPa\,s^{-1}$ and strongly divergent 250-hPa irrotational wind vectors in the equatorward entrance of the NPJ. The 250-hPa irrotational wind vectors are directed poleward from regions of low PV air to regions of high PV air within the entrance region of the NPJ and are parallel to the direction of the upper-tropospheric ageostrophic wind (not shown). The upper-tropospheric outflow therefore acts to increase the rate at which air parcels accelerate into the entrance region of the NPJ. The orientation and gradient of the irrotational flow relative to the horizontal PV gradient is also consistent with an increase in the magnitude of the upper-tropospheric PV gradient via PV frontogenesis (e.g., Davies and Rossa 1998). These processes are related to the quasi-stationary characteristic and concomitant intensification of the NPJ over the East China Sea near 35°N, 120°E between 20 and 21 October 2010 (Figs. 5a,b), and over the central North Pacific near 35°N, 170°E between 22 and 23 October 2010 (Figs. 5c,d). The quasi-stationary and intensifying characteristics of the NPJ are similar to the quasi-stationary, ''backbuilding,'' and intensifying characteristics of a jet streak observed in conjunction with troposphere-deep convection over the United States within three PREs documented by Bosart et al. (2012).

The AR_1 and AR_2 both develop in environments characterized by weak 700-hPa frontogenesis $<2\,K\,(100\,km)^{-1}\,day^{-1}$ and weak QG forcing for ascent associated with 700-hPa **Q**-vector convergence greater than $-2\times10^{-12}\,Pa\,m^{-2}\,s^{-1}$ on 20 and 22 October 2010, respectively (Figs. 6a,c). However, as the AR_1 and AR_2 continue to meridionally contract and extend eastward on 22 and 23 October 2010, respectively, they cross the date line in environments characterized by midtropospheric frontogenesis $>8\,K\,(100\,km)^{-1}\,day^{-1}$ and QG forcing for ascent associated with **Q**-vector convergence values less than $-6\times10^{-12}\,Pa\,m^{-2}\,s^{-1}$ on (Figs. 6b,d). The ARs are located equatorward of the regions of strongest midtropospheric frontogenesis, indicative of the poleward-tilt of partial IVT and transition to a baroclinic environment observed in Fig. 4 and discussed in section 3. During this latter period of AR evolution, the orientation of the **Q** vectors are directed toward regions of higher (warmer) potential temperature at 700 hPa, indicative of regions of lower-tropospheric geostrophic frontogenesis and a strong thermally direct ageostrophic circulation in the entrance region of the NPJ (Figs. 6c,d).

b. Cross-sectional perspectives

The cross sections in Fig. 7 illustrate the vertical structure of the dynamical quantities discussed in section 4a. These quantities include the vertical distributions of upward vertical motion, frontogenesis, ageostrophic circulation vectors, and CAPE for transects as in Fig. 4. The lower-tropospheric water vapor mixing ratio, upper-tropospheric wind speed, and potential temperature fields from Fig. 4 are reproduced. The AR_1 is initially located in a region primarily characterized by troposphere-deep upright ascent and weak frontogenesis beneath the equatorward entrance region of the NPJ on 20 October

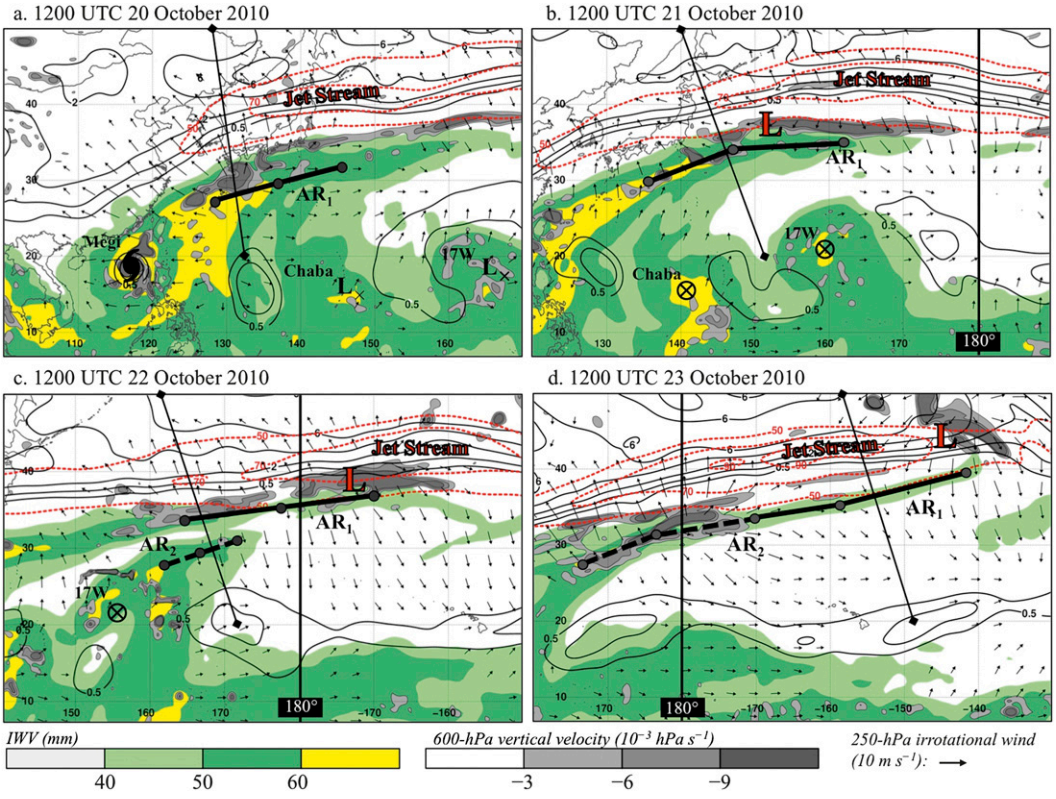

FIG. 5. IWV (mm; shaded according to the green–yellow color bar), 600-hPa upward vertical motion (10^{-3} hPa s^{-1}; shaded according to the gray color bar), 250-hPa wind speed (red dashed contours every 10 m s^{-1} beginning at 50 m s^{-1}), 250-hPa potential vorticity [solid black contours at 0.5 potential vorticity units (PVU, 1 PVU = 10^{-6} K kg^{-1} m^2 s^{-1}), 1.0 PVU, and every 1.0 PVU thereafter], and 250-hPa irrotational wind (m s^{-1}; vectors plotted with a magnitude >2 m s^{-1} with reference magnitude in lower right of image) at 1200 UTC on (a)–(d) 20–23 Oct 2010. The endpoints and midpoint of AR_1 and AR_2 are labeled and indicated by the heavy lines. The locations of TCs Megi, Chaba, 17W, and the frontal low are indicated with symbols as in prior figures. The date line is prominently labeled to highlight that the domain shifts eastward over time. Barbell lines pertain to cross-sectional analyses in Figs. 4 and 7. The data source is the NCEP CFSR.

2010 (Fig. 7a). The AR_1 is subsequently located in a region characterized by both upright ascent and sloped ascent on 21 October 2010 (Fig. 7b). The sloped ascent regions in the middle and upper troposphere correspond to regions of sloped frontogenesis with a magnitude >2 K (100 km)$^{-1}$ day^{-1} (Fig. 7b), whereas the upright ascent regions correspond to regions of CAPE values >1000 J kg^{-1} (Fig. 7e)[3] and regions of lower-tropospheric mixing ratio values >15 g kg^{-1} (Figs. 7a,b). The regions of troposphere-deep sloped frontogenesis correspond to a thermally direct ageostrophic circulation in the plane of the cross section on 20 and 21 October 2010 (Figs. 7a,b).

The AR_2 is initially located in a region characterized by troposphere-deep upright and sloped ascent in the equatorward entrance region of the NPJ on 22 October 2010 (Fig. 7c). The sloped ascent regions correspond to regions of sloped frontogenesis with a magnitude >3 K (100 km)$^{-1}$ day^{-1} (Fig. 7b), whereas the upright ascent regions correspond to regions of CAPE values >2000 J kg^{-1} (Fig. 7e) and regions of lower-tropospheric mixing ratio values >15 g kg^{-1} (Fig. 8c). The AR_2 is subsequently located in a region characterized by lower- and midtropospheric sloped ascent equatorward of the NPJ on 23 October 2010 (Fig. 7d), corresponding to regions of sloped frontogenesis with a magnitude >6 K (100 km)$^{-1}$ day^{-1}. The AR_2 is located within an environment characterized by CAPE values <500 J kg^{-1} (Fig. 7e). The regions of sloped frontogenesis on 22 and 23 October 2010 correspond to a lower- and midtropospheric thermally direct ageostrophic circulation in the plane of the cross section (Figs. 7c,d). The above-described changes in upward vertical motion, CAPE, and frontogenesis following AR_1 and AR_2 are consistent with

[3] Observed CAPE values > 1000 J kg^{-1} over portions of the subtropical western North Pacific are not uncommon in October (e.g., Riemann-Campe et al. 2009).

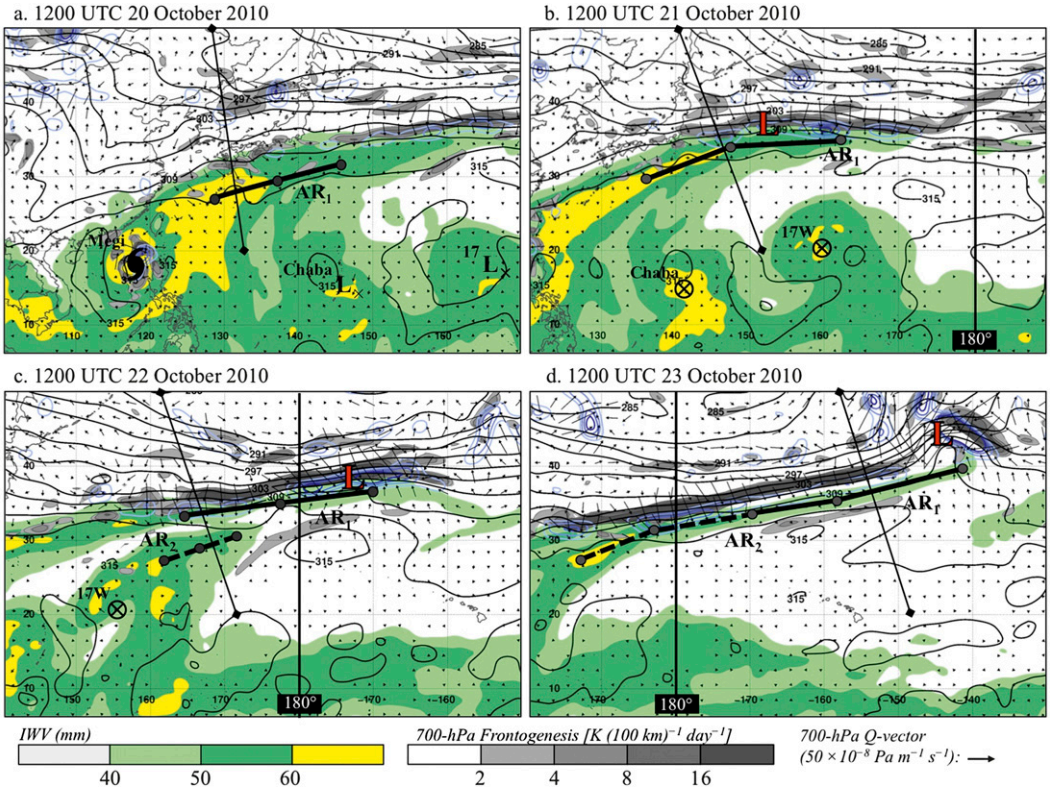

FIG. 6. IWV (mm; shaded according to the green–yellow colorbar), 700-hPa potential temperature (solid contours every 3 K), 700-hPa horizontal frontogenesis [K (100 km)$^{-1}$ day^{-1}; shaded according to the gray colorbar], 700-hPa **Q** vectors (10^{-8} Pa m^{-1} s^{-1}; reference magnitude in lower right of image), and 700-hPa **Q**-vector divergence (increasingly negative values contoured from light blue to dark blue every 2×10^{-12} Pa m^{-2} s^{-1}) at 1200 UTC on (a)–(d) 20–23 Oct 2010. Labeling convention and data source are as in Fig. 5.

a transition from a tropical environment to an extratropical environment as discussed in section 3c. The evolution from upright to sloped upward vertical motion following AR_1 and AR_2 further suggests the ARs become coupled to the thermally direct ageostrophic circulation in the entrance region of the NPJ and that they likely overlap with a portion of the warm conveyor belt.

c. *Average environmental conditions along ARs*

The average IWV, IVT, CAPE, 925–700-hPa frontogenesis, and terms in the water vapor budget from Eq. (5) are computed for AR_1 at 1200 UTC on 20 and 22 October 2010, for AR_2 at 1200 UTC on 22 and 23 October 2010, and for the merged AR phase at 1200 UTC 24 October 2010. Each quantity is averaged along the AR corridors drawn in Figs. 6 and 7 and are the arithmetic average of all grid points within ±1° latitude of each AR corridor. The AR corridors are defined using a combination of IWV values >40 mm and IVT magnitude >400 kg m^{-1} s^{-1}. The IWV values (and IVT magnitudes) associated with each AR decrease or remain constant (increase) between the development and evolution phases (Table 1). The increase in IVT, despite coincident decreases in IWV, is associated with an increase in the vertically averaged mean horizontal wind speed from <10 m s^{-1} on 20 October 2010 to >25 m s^{-1} on 24 October 2010 (not shown). The ARs are also initially located in environments characterized by large CAPE values >1000 J kg^{-1} (Table 1) that likely contributed to troposphere-deep upright ascent (Fig. 7), poleward-directed upper-tropospheric diabatic outflow (Fig. 5), and the increase in the magnitude of the NPJ (Fig. 3). As a result, the ARs were subsequently located in environments characterized by regions of area-averaged 925–700-hPa frontogenesis >5 K (100 km)$^{-1}$ day^{-1} (Table 1) and area-averaged 700-hPa QG forcing for ascent associated with **Q**-vector convergence $< -0.5 \times 10^{-12}$ Pa m^{-2} s^{-1} (not shown; see Fig. 6).

The precipitation rate along the AR_1 corridor is initially 35.0 mm day^{-1} and the IVT convergence along the AR_1 corridor is 16.3 mm day^{-1} on 20 October 2010 (Table 2). The resulting IWV tendency is −16.8 mm day^{-1} and is consistent with IWV removal via saturated ascent and large precipitation rates. The precipitation rate along

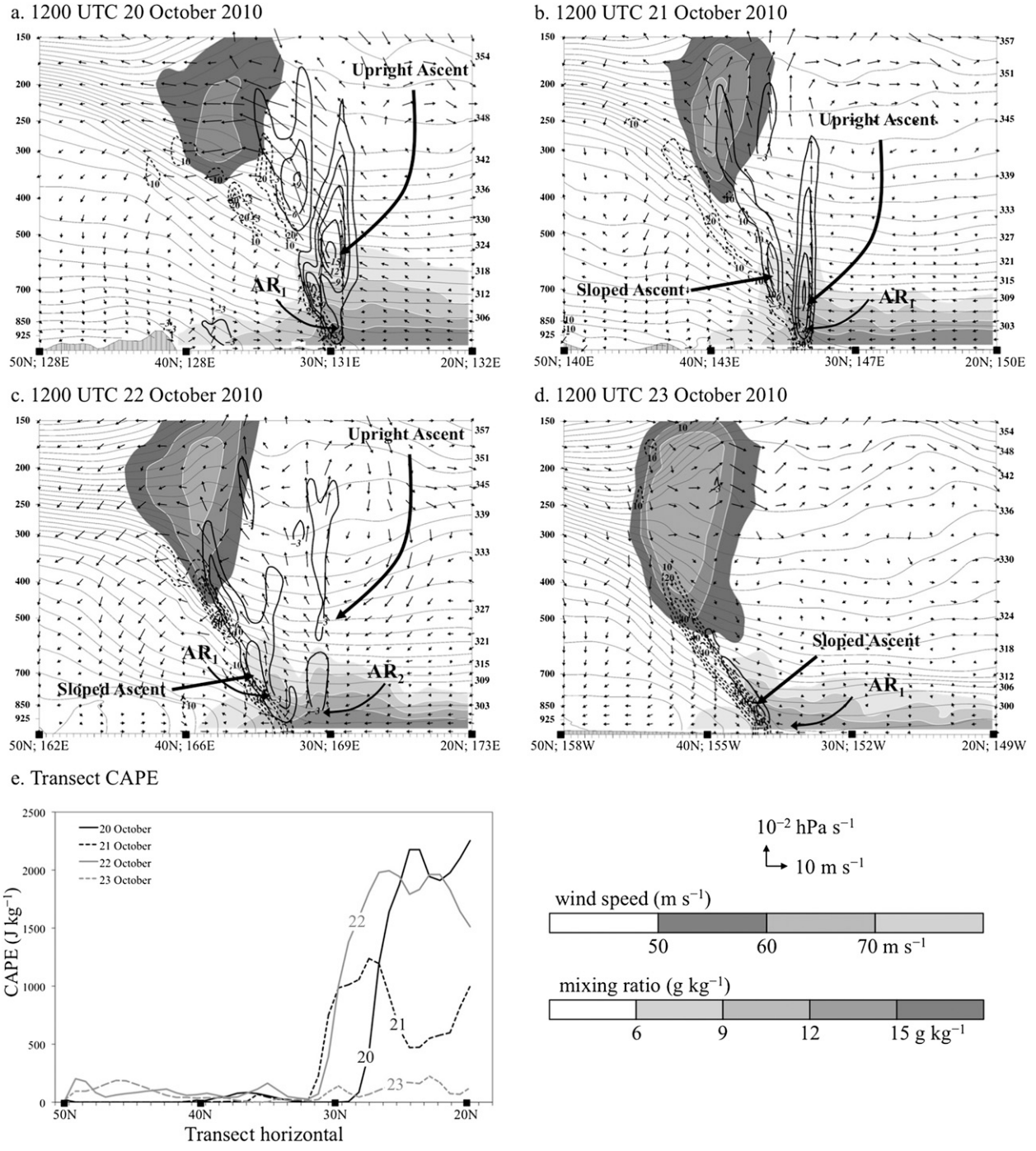

FIG. 7. Cross sections of horizontal wind speed (dark-to-light shade for values $>50\,\mathrm{m\,s^{-1}}$), mixing ratio (light-to-dark shade for values $>6\,\mathrm{g\,kg^{-1}}$), two-dimensional frontogenesis [dashed contours every $10\,\mathrm{K\,(100\,km)^{-1}\,day^{-1}}$ starting at $10\,\mathrm{K\,(100\,km)^{-1}\,day^{-1}}$], potential temperature (K; solid gray contours labeled along right vertical axis), upward vertical motion (solid contours every $3 \times 10^{-3}\,\mathrm{hPa\,s^{-1}}$), and ageostrophic circulation vectors in the plane of the cross section (horizontal component in $\mathrm{m\,s^{-1}}$ and vertical component in $\mathrm{hPa\,s^{-1}}$; reference vectors shown at bottom right) at 1200 UTC on (a)–(d) 20–23 Oct 2010. (e) Transect CAPE ($\mathrm{J\,kg^{-1}}$) is provided. Cross-sectional lines are provided in Figs. 4, 5, and 6. Pressure is labeled along left vertical axis in hPa. The data source is the NCEP CFSR.

TABLE 1. Area-averaged IWV (mm), IVT (kg m^{-1} s^{-1}), CAPE (J kg^{-1}), and 925–700-hPa layer-mean two-dimensional frontogenesis [K (100 km)$^{-1}$ day^{-1}] along AR corridors. The area-average is the mean of all gridpoint data locations within ±1° latitude of each AR corridor (see text). The data source is the NCEP CFSR dataset.

AR	Day (1200 UTC)	IWV (mm)	IVT (kg m^{-1} s^{-1})	CAPE (J kg^{-1})	Frontogenesis [K (100 km)$^{-1}$ day^{-1}]
AR_1	20 Oct	57.7	425.0	1333.9	0.2
	22 Oct	49.0	923.0	130.5	8.5
AR_2	22 Oct	53.0	752.9	1897.6	0.2
	23 Oct	54.8	1002.8	653.6	8.4
Merged	24 Oct	52.6	1050.1	5.5	2.3

the AR_1 corridor subsequently decreases, whereas the IVT convergence is approximately constant. The evaporation rate also increases along the AR_1 corridor, and the resulting IWV tendency increases to 0.8 mm day^{-1} at 1200 UTC 22 October 2010. The decrease in the precipitation rate and constant IVT convergence along the AR_1 corridor is consistent with a transition from an environment characterized by tropospheric-deep upward vertical motion to an environment characterized by poleward-tilted sloped ascent in the presence of strong frontogenesis. The terms in the water vapor budget along the AR_2 corridor are less defined as the water budget tendencies for AR_1 given its short life cycle prior to merging with AR_1 over the eastern North Pacific. The IWV tendency along the AR_2 corridor is 23.3 mm day^{-1} at 1200 UTC 22 October 2010 primarily in association with large IVT convergence values, whereas the IWV tendency is −1.4 mm day^{-1} at 1200 UTC 23 October 2010 in association with large precipitation rates and IVT convergence.

5. Trajectory analysis

An air parcel trajectory analysis is provided in order to assess the origination and termination locations of air parcels that are collocated with AR_1 and AR_2 (Figs. 8 and 9, respectively). The analysis is limited to the time periods that correspond to the development of the ARs and time periods representative of their evolution across the North Pacific prior to landfall. Kinematic backward and forward air parcel trajectories are computed from locations at 950 hPa on a 1° latitude × 1° longitude grid for locations with IWV values >40 mm and IVT values >400 kg m^{-1} s^{-1} centered near the midpoint of each AR corridor drawn in Figs. 6 and 7. The horizontal and vertical locations of air parcels are linearly interpolated with a 1-h time step from the horizontal and vertical wind components in the 6-hourly NCEP CFSR reanalysis. The water vapor mixing ratio and potential temperature following the trajectories are analyzed every 6 h at CFSR reanalysis times. A Lagrangian form of the water vapor budget shown in section 2 is also analyzed every 6 h as $d[\mathrm{IWV}]/(dt) = E - P$ following a methodology similar to Stohl and James (2004).

a. Development and evolution of AR_1

The time of AR_1 development t_d is set at 1200 UTC 20 October 2010. The AR_1 at $t_d + 0$ h comprises air parcels located at 950 hPa that originate in the lower troposphere at or below 900 hPa to the east of TC Megi and to the northwest of TC Chaba at $t_d - 72$ h (1200 UTC 17 October 2010; Fig. 8a). These air parcels are characterized by IWV values >50 mm (Fig. 8a) at $t_d - 72$ h and maintain these IWV values at $t_d + 0$ h (Figs. 8a,b). Air parcels subsequently proceed along two trajectory paths between $t_d + 0$ and $t_d + 72$ h (1200 UTC 23 October 2010; Fig. 8c). Air parcels either remain in the lower troposphere below 700 hPa and travel to the west within the lower-tropospheric cyclonic circulation of TC Megi or rapidly ascend into the upper troposphere above

TABLE 2. Area-averaged precipitation rate (mm day^{-1}), IVT convergence (mm day^{-1}), evaporation rate (mm day^{-1}), and IWV tendency (mm day^{-1}) along AR corridors. The area-average is the mean of gridpoint data locations within ±1° latitude of each AR corridor (see text). The data sources are the NCEP CFSR and NASA TRMM dataset.

AR	Day (1200 UTC)	Precipitation (mm day^{-1})	IVT convergence (mm day^{-1})	Evaporation (mm day^{-1})	IWV tendency (mm day^{-1})
AR_1	20 Oct	35.0	16.3	2.0	−16.8
	22 Oct	26.0	18.0	8.8	0.8
AR_2	22 Oct	4.1	22.6	4.7	23.3
	23 Oct	60.3	51.6	7.3	–1.4
Merged	24 Oct	7.8	–3.8	1.6	–10.1

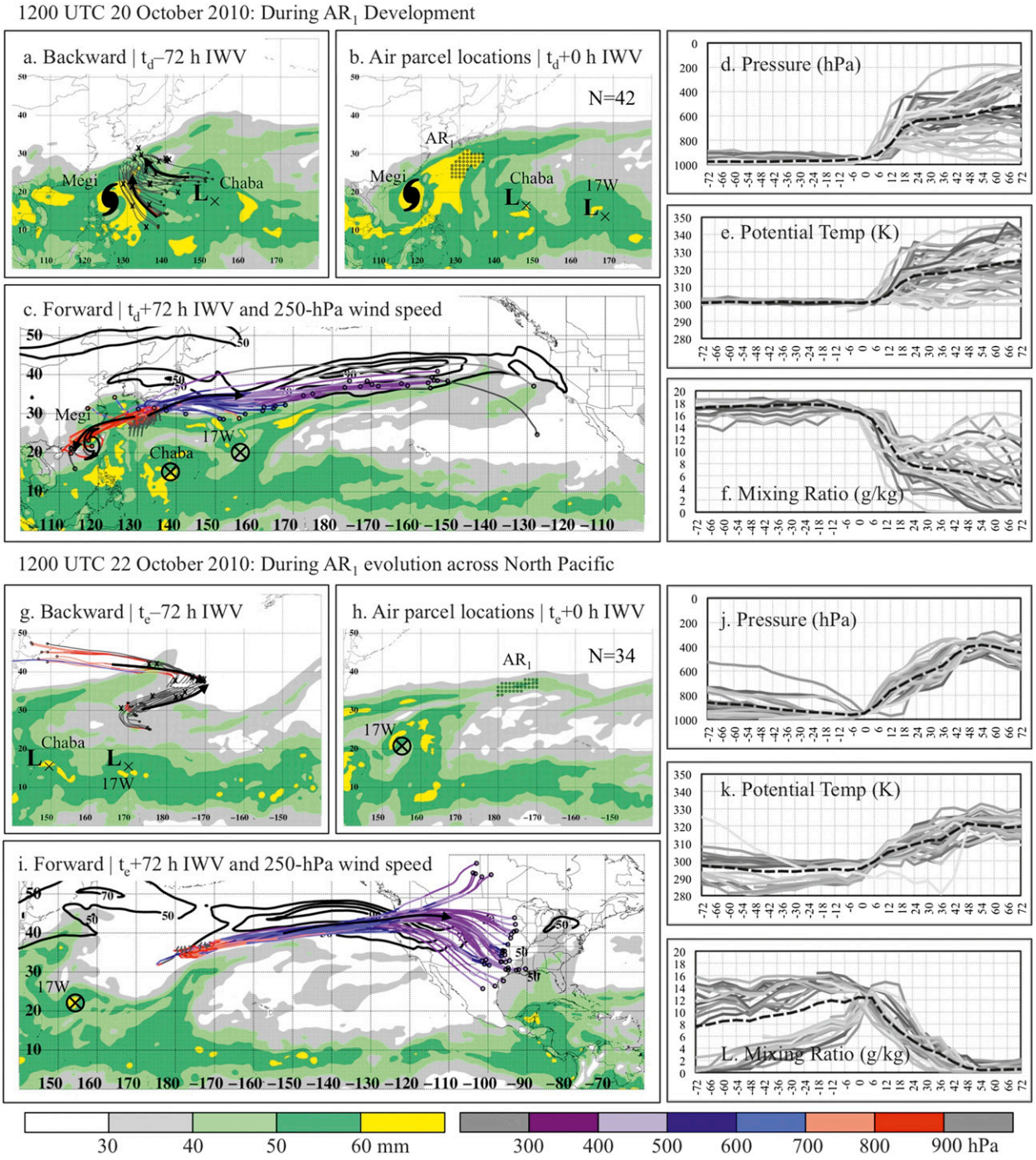

FIG. 8. AR_1 trajectories: (a)–(f) 72-h backward and forward air parcel trajectories for air parcels terminating at 950 hPa at the development time t_d of AR_1 at 1200 UTC 20 Oct 2010. Panels include (a) 72-h backward air parcel trajectories overtop $t_d - 72$ h IWV (mm; shaded) and 250-hPa wind speed (contours every 10 m s^{-1} beginning at 50 m s^{-1}); (b) locations of air parcel trajectories at $t_d + 0$ h based on IWV > 40 mm and IVT > 400 kg m^{-1} s^{-1}; (c) as in (a), but for 72-h forward air parcel trajectories overtop $t_d + 72$ h IWV and 250-hPa wind speed; (d) parcel pressure (hPa); (e) parcel potential temperature (K); and (f) parcel mixing ratio (g kg^{-1}). (g)–(l) As in (a)–(f), but for 72-h backward and forward air parcel trajectories for air parcel terminating at 950 hPa at the evolution time t_e of AR_1 at 1200 UTC 22 Oct 2010. Trajectories are shaded according to parcel pressure and are not drawn if they attain a pressure value >1000 hPa (marked by an "×"). Trajectory endpoints contain white-filled circles. The locations of tropical cyclones are noted as in prior figures. The data source is the NCEP CFSR.

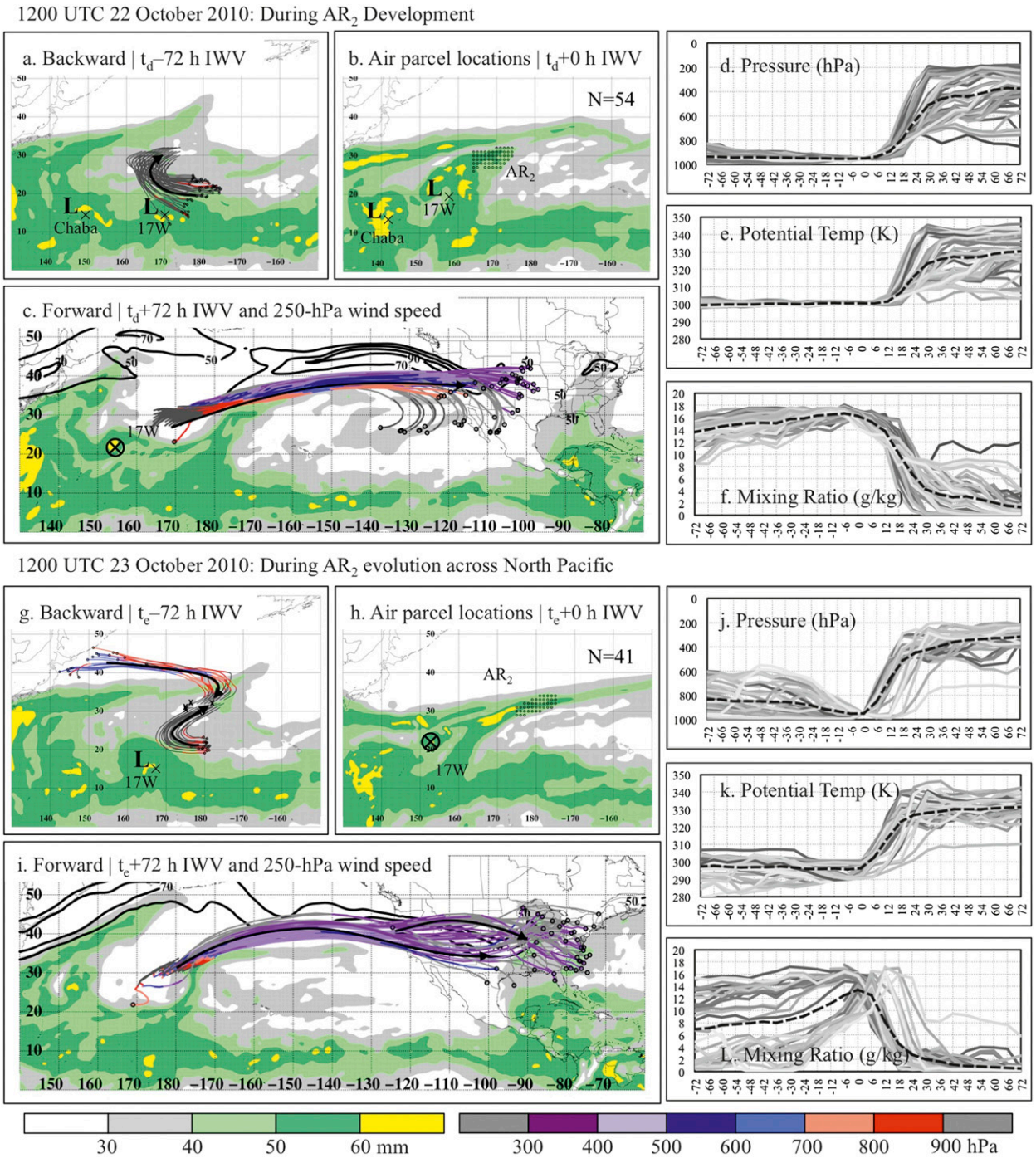

FIG. 9. AR_2 trajectories: As in Fig. 8, but for 72-h backward and forward air parcel trajectories for air parcels terminating at 950 hPa at (a)–(f) the development time t_d of AR_2 at 1200 UTC 22 Oct 2010 and (g)–(l) the evolution time t_e of AR_2 at 1200 UTC 23 Oct 2010.

400 hPa and travel to the east along the anticyclonic shear side of the jet stream (Figs. 8c,d). The air parcels that rapidly ascend into the upper troposphere are associated with average increases in potential temperature >30 K (Fig. 8e) and average decreases in water vapor mixing ratio $>15\ g\ kg^{-1}$ (Figs. 8f). These changes in air parcel pressure, potential temperature, and water vapor mixing ratio are consistent with periods of saturated ascent, diabatic heating via condensation, and large precipitation rates during the period of AR_1 development.

The time of AR_1 evolution t_e over the North Pacific is analyzed at 1200 UTC 22 October 2010 (Figs. 8g–l). The AR_1 at $t_e + 0$ h comprises air parcels located at 950 hPa that originate in the subtropical lower troposphere at or below 900 hPa near 30°N, 170°E; and in the extratropical midtroposphere at ~700 hPa near 45°N, 150°E, at $t_e -$ 72 h (1200 UTC 19 October 2010; Fig. 8g). These air parcels are initially characterized by IWV values <40 and <30 mm at $t_e - 72$ h, respectively (Fig. 8g), and are later characterized by IWV values >40 mm at $t_e + 0$ h (Fig. 8h). The confluent air parcel trajectories between $t_e - 72$ and $t_e + 0$ h (Fig. 8g) are suggestive of increasing frontogenesis (Table 1) and IVT convergence (Table 2) along the AR corridor. Air parcels subsequently proceed along one trajectory path between $t_e + 0$ and $t_e + 72$ h (1200 UTC 25 October 2010; Fig. 8i). Air parcels generally ascend into the upper troposphere to ~400 hPa, travel to the east along the corridor of the upper-tropospheric jet stream, and contain diffluent trajectory paths over western North America within the exit region of the upper-tropospheric jet stream (Figs. 8i,j). These air parcel are associated with average increases in potential temperature >20 K (Fig. 8k) and average decreases in water vapor mixing ratio of ~12 g kg^{-1} (Figs. 8l). These later changes in parcel pressure, potential temperature, and water vapor mixing ratio are consistent with periods of less robust upward vertical motion, diabatic heating via condensation, and precipitation rates (cf. AR_1 development) during the evolution of the AR across the North Pacific, and may be consistent with more sloped air parcel ascent as compared to upright air parcel ascent. The air parcels that originate in the extratropical midtroposphere are associated with increasing mixing ratio values as they descend to 950 hPa between $t_e - 72$ and $t_e + 0$ h, whereas the air parcels that originate in the subtropics exhibit relatively constant mixing ratio values (Figs. 8j,l).

b. Development and evolution of AR_2

The time of AR_2 development t_d is set at 1200 UTC 22 October 2010. The AR_2 at $t_d + 0$ h comprises air parcels located at 950 hPa that originate in the lower troposphere at or below 900 hPa to the east of TC 17W at $t_d - 72$ h (1200 UTC 19 October 2010; Fig. 9a). These air parcels are initially characterized by IWV values between 30 and 50 mm (Fig. 9a) at $t_d - 72$ h and are later characterized by IWV values between 40 and 50 mm at $t_d + 0$ h (Figs. 9a,b). A majority of air parcels subsequently ascend into the upper troposphere above 400 hPa and travel to the east within the upper-tropospheric jet stream between $t_d + 0$ and $t_d + 72$ h (1200 UTC 25 October 2010; Figs. 9c,d). The air parcels that ascend into the upper troposphere are associated with average increases in potential temperature >30 K (Fig. 9e) and average decreases in water vapor mixing ratio >15 g kg^{-1} (Figs. 9f). Similar to the development of AR_1, these changes in air parcel pressure, potential temperature, and water vapor mixing ratio are consistent with periods of saturated ascent, diabatic heating via condensation, and large precipitation rates during the period of AR_2 development.

The time of AR_2 evolution t_e over the North Pacific is analyzed at 1200 UTC 23 October 2010 (Figs. 9g–l), immediately prior to the merger of the two ARs. The AR_2 at $t_e + 0$ h comprises air parcels located at 950 hPa that originate in the subtropical lower troposphere at or below 900 hPa near 22°N, 180°, and in the extratropical middle troposphere at ~650 hPa near 45°N, 155°E, at $t_e - 72$ h (1200 UTC 20 October 2010; Fig. 9g). These air parcels are initially characterized by IWV values <40 and <30 mm, respectively, at $t_e - 72$ h (Fig. 9g) and are later characterized by IWV values >40–50 mm at $t_e +$ 0 h (Fig. 9h). Air parcels subsequently ascend into the upper troposphere above 400 hPa, travel to the east along the corridor of the upper-tropospheric jet stream, and contain diffluent trajectory paths over central North America within the exit region of the upper-tropospheric jet stream between $t_e + 0$ and $t_e + 72$ h (1200 UTC 26 October 2010; Figs. 9i,j). These air parcel are associated with average increases in potential temperature of ~20 K (Fig. 9k) and average decreases in water vapor mixing ratio of ~12 g kg^{-1} (Figs. 9l). The confluent air parcel trajectories between $t_e - 72$ to $t_e + 0$ h (Fig. 9g) are strongly suggestive of increasing frontogenesis (Table 1) and IVT convergence (Table 2) along the AR corridor, whereas the later changes in potential temperature and water vapor mixing ratio are consistent with periods of weak saturated ascent, diabatic heating via condensation, and precipitation during the evolution of AR_2 across the North Pacific. The air parcels that originate in the extratropical midtroposphere are associated with increasing mixing ratio values as they descend to 950 hPa between $t_e - 72$ and $t_e + 0$ h (Figs. 9j,l).

c. Lagrangian water vapor budget

An IWV tendency is estimated from the Lagrangian form of the water vapor budget following air parcels in the trajectory analysis from 36 h before to 36 h after the trajectory initialization time (hereafter referred to as "t" to collectively represent t_d or t_e). The terms are estimated as the average value of each quantity at all air parcel locations every 6 h from the NCEP CFSR and NASA TRMM datasets (see section 2). The average Lagrangian IWV tendency at all air parcel locations that comprise either the AR corridor during the development and evolution phases is generally near zero or negative from $t - 36$ to $t - 12$ h and strongly negative

from $t - 12$ to $t + 36$ h (Fig. 10). The general trends observed in the Lagrangian IWV tendency are consistent with horizontal transport of water vapor (e.g., near-zero IWV tendency) and removal of water vapor via ascent and precipitation (e.g., negative IWV tendency) following air parcels paths. At most time periods, the precipitation rate is much larger than the evaporation rate.

The Lagrangian form of the water vapor budget indicates that the locations of air parcels largely are associated with constant IWV values before their aggregation along the AR corridor and decreasing IWV values after their aggregation along the AR corridor. In the Eulerian framework, however, the horizontal aggregation of individual air parcels along the AR corridor is associated with average magnitudes of the IVT convergence term $>45\,\text{mm day}^{-1}$ during the AR development phase (Figs. 10a,c) and between 30 and $45\,\text{mm day}^{-1}$ during the AR evolution phase (Figs. 10b,d). The lagged IVT convergence maxima in Fig. 10 suggests that the average *Eulerian* IWV tendency is strongly influenced by the horizontal aggregation of water vapor along the AR corridor during the evolution phase, and less so during the development phase. A similar lagged response in the average precipitation rate suggests that air parcels residing along the AR corridor may ascend and produce precipitation at a faster rate during the evolution phase as compared to the development phase. The lagged responses are representative of the air parcel residence times within environments meeting the AR criteria (IWV >40 mm and IVT $>400\,\text{kg m}^{-1}\,\text{s}^{-1}$). The air parcels are more likely to reside within environments with large IWV values and IVT magnitudes prior to and during the AR development phase (~18–30 h) as compared to the AR evolution phase (~6–12 h). Evaporation is not a large contribution to the average Lagrangian IWV tendency; however, during select time periods evaporation from the surface may act to increase or decrease the IWV tendency when the precipitation rate is small. Small differences in the IWV tendency and terms in the Lagrangian water vapor budget are observed for air parcels that originate in the extratropics versus those that originate in the subtropics during the evolution phases of the two ARs (not shown). The largest differences between the two groups of air parcels is the evaporation rate, which is approximately 30% larger following air parcels that originate in the extratropical midtroposphere and descend into the lower troposphere along the AR corridor (not shown). These differences are consistent with increase in water vapor mixing ratio along air parcel trajectories that originate in the extratropics (Figs. 8l and 9l).

6. Synthesizing discussion

a. Dynamical summary

A schematic overview for the development and evolution of two zonally elongated ARs in this study is provided in Fig. 11. The two ARs in this study developed near western North Pacific TCs Megi, Chaba, and 17W in association with water vapor transport from regions of IWV $>$ 50–60 mm near the TCs. The two ARs developed within high-CAPE environments in the equatorward entrance region of an intensifying NPJ that supported troposphere-deep air parcel ascent, large diabatic heating and precipitation rates, and upper-tropospheric diabatic outflow that geographically anchored and intensified the NPJ over the western and central North Pacific (Figs. 11a,b). The IWV associated with each AR (primarily AR_1) decreased during the period of development in association with large precipitation rates. The strong thermally direct ageostrophic circulation that developed beneath the entrance region of the NPJ was subsequently associated with troposphere-deep sloped frontogenesis and IVT convergence that offset the deleterious effect of precipitation on the IWV tendency during the period of AR evolution over the central North Pacific (Figs. 11c,d). Although the ARs initially developed in conjunction with water vapor largely transported from regions near western North Pacific TCs and in the presence of large precipitation rates, the subsequent evolution of the ARs occurred in conjunction with water vapor transported from the extratropics and subtropics in the presence of frontogenesis and IVT convergence over the central and eastern North Pacific (Fig. 11e). The landfall of the zonally elongated and merged AR subsequently produced widespread heavy precipitation (>50 mm; maxima of >200 mm) at many locations across coastal and interior Northern California, Oregon, and Washington (Fig. 11e).

b. Similarities to predecessor rain events

The development of the two ARs in this study share several similarities with PRE formation documented in the studies outlined in section 1. The ARs described in this study, and PREs documented in previous studies, developed in association with water vapor transported from regions near a TC within high-CAPE environments and contained air parcels that experienced troposphere-deep ascent into the upper troposphere. The ARs also developed and evolved across the North Pacific within the thermally direct frontogenetical ageostrophic circulation beneath the equatorward entrance region of a quasi-stationary and intensifying upper-tropospheric jet streak. As seen in case studies, composite analyses, and numerical modeling studies of PREs (e.g., Schumacher

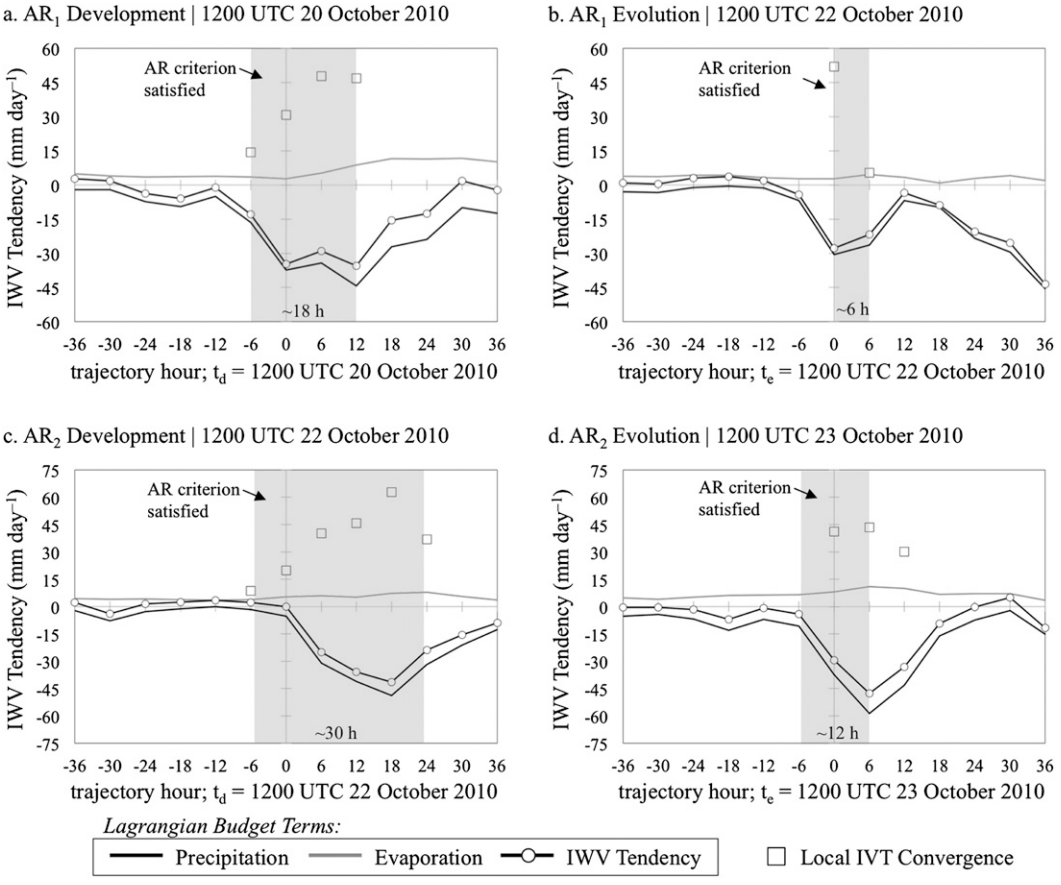

FIG. 10. Average contributions to the IWV tendency from the Lagrangian form of the water vapor budget following air parcel trajectories from Figs. 8 and 9 for the 36 h before and 36 h after the (a) development time of AR_1 at 1200 UTC 20 Oct 2010, (b) evolution time of AR_1 at 1200 UTC 22 Oct 2010, (c) development time of AR_2 at 1200 UTC 22 Oct 2010, and (d) evolution time of AR_2 at 1200 UTC 23 Oct 2010. Contributions include precipitation rate (mm day^{-1}; solid) and evaporation rate (mm day^{-1}; gray). The IWV tendency (mm day^{-1}) is plotted as a solid line with circle markers. The average IVT convergence (mm day^{-1}; square markers) is shown when air parcels were located in "AR" environments containing IWV > 40 mm and IVT > 400 kg m^{-1} s^{-1} (shaded). The average values represent the arithmetic mean of values at all air parcel locations at a given time lag relative to t_d or t_e.

et al. 2011; Bosart et al. 2012; Moore et al. 2013) and recurving western North Pacific TCs (e.g., Archambault et al. 2013), the current analysis also illustrated troposphere-deep air parcel ascent and coincident upper-tropospheric diabatic outflow that contributed to an intensification and "back building" evolution of the upper-tropospheric jet.

The relative importance of the TCs and the upper-tropospheric diabatic outflow is demonstrated by Schumacher et al. (2011), who show that the upper-tropospheric diabatic outflow in the entrance region of an upper-tropospheric jet streak is reduced in a model simulation in which a tropical water vapor plume is removed (see their Fig. 18a). Similar results for the case with and without a recurving western North Pacific TC are shown in Grams et al. (2013). The presence of a PRE or TC can have a potentially large influence on the structure and evolution of the upper-tropospheric jet. In the present study, the TCs likely contributed to AR development in association with the poleward transport of tropical water vapor into the subtropics. The diabatic outflow in the equatorward entrance region of an intensifying upper-tropospheric jet streak associated with the TCs and the PRE-like AR development also likely contributed to AR evolution in association with the development of a strong thermally direct ageostrophic circulation and concomitant IVT convergence along the AR corridors.

NASA's TRMM estimates of the average precipitation rates were ~5–60 mm day^{-1} along the AR corridors (Table 2) and were ~0–60 mm day^{-1} following air parcels (Fig. 10) comprising the ARs during the AR

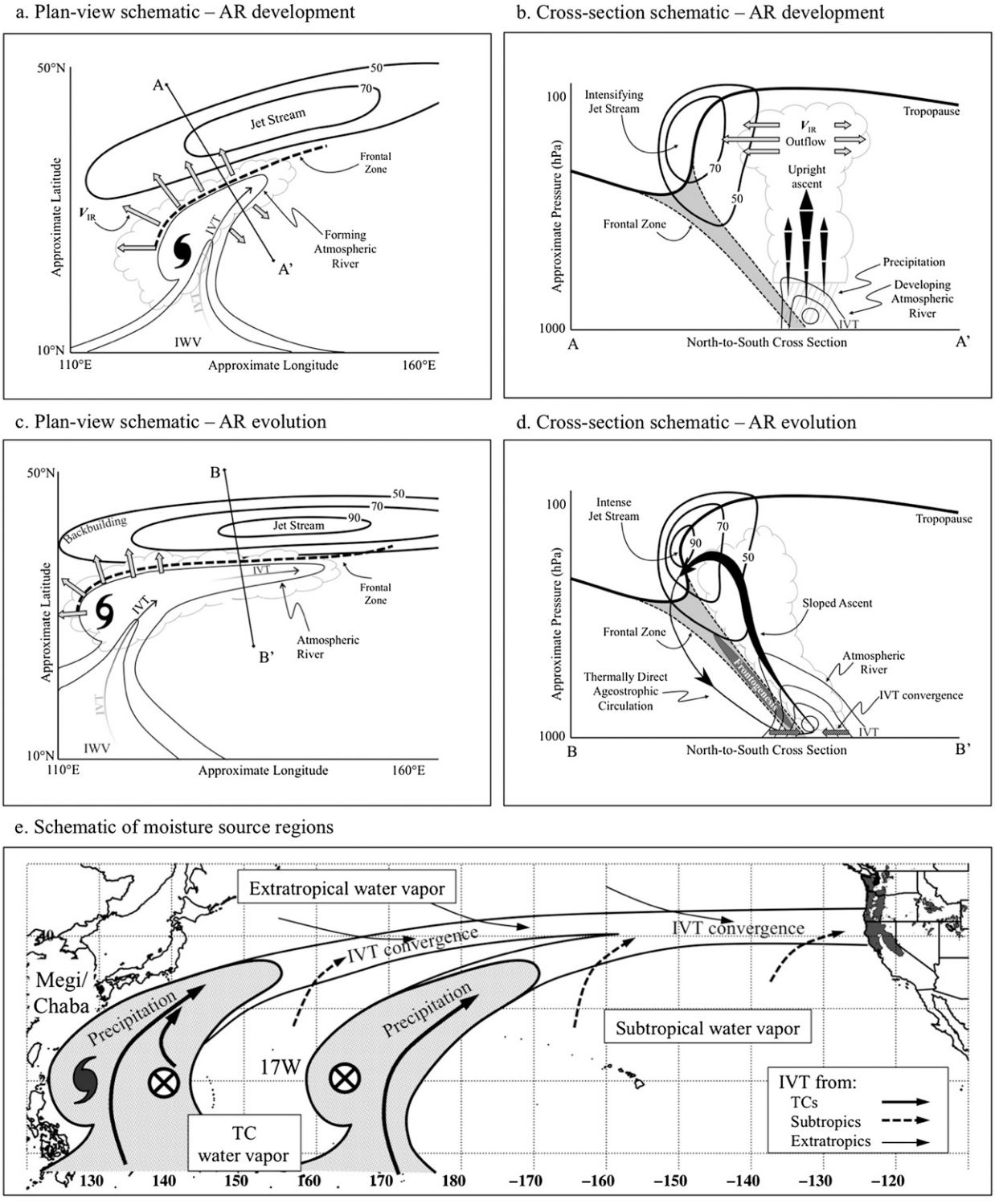

FIG. 11. Schematics representation of the (a) horizontal and (b) vertical structure of AR development in association with water vapor transport from a TC in the equatorward entrance region of an intensifying upper-tropospheric jet streak in the presence of precipitation, and of the (c) horizontal and (d) vertical structure of AR evolution in association with frontogenesis and a strong thermally direct ageostrophic circulation within the equatorward entrance region of an intense upper-tropospheric jet streak in the presence of IVT convergence; (b) and (d) are modeled after Shapiro (1982). (e) An overview of water vapor source regions during AR development (i.e., tropical source regions) and during AR evolution (i.e., subtropical and extratropical source regions). The 48-h accumulated precipitation ending at 1200 UTC 25 Oct 2010 from Fig. 1d is contoured and shaded in gray above 50 mm over the western United States.

development and evolution phases. NASA's TRMM estimates of the instantaneous precipitation rate for individual locations along the AR corridors and individual air parcels were $>100\,\text{mm day}^{-1}$ on 20–22 October 2010 (not shown). Observed precipitation totals over coastal and interior regions of Northern California also exceeded $100\,\text{mm day}^{-1}$ with many locations receiving 200 mm over a 2-day period (Fig. 1d). Evidence suggests that the development phases of the ARs may have been associated with PRE development based on the transport of water vapor from TC source regions and instantaneous precipitation estimates from NASA's TRMM dataset of $>100\,\text{mm day}^{-1}$; however, the precipitation event produced by the subsequent evolution of the ARs and landfall of the merged AR cannot be considered a PRE as it did not occur in conjunction with water vapor transport *directly* from a TC. Although observational evidence indicates that not all PREs are associated with the formation of ARs, the aforementioned atmospheric processes associated with the formation of PREs were particularly conducive to the development of the two ARs over the North Pacific in October 2010. Future work is aimed at investigating what fraction of TCs and PREs over the western North Pacific may be associated with the subsequent development of ARs and whether or not these ARs increase or decrease our ability to better predict extreme rain events along the U.S. West Coast.

c. *Implications of results*

The results of this study demonstrate that AR formation over the western North Pacific can occur in association with poleward water vapor transport from TCs. This process is similar to a tropical moisture export from a TC described in Knippertz et al. (2013). The processes described for AR formation in this study also complements research that describes the formation of AR-like features downstream of upper-tropospheric subtropical troughs at low latitudes (e.g., McGuirk et al. 1987; Waugh and Funatsu 2003; Knippertz 2007; Ralph et al. 2011). The results herein indicate that AR-like features may also form in the absence of an upstream subtropical trough given sufficient poleward water vapor transport into the midlatitudes on the east and poleward side of a TC. The air parcel trajectory analysis also suggests that the two ARs in this study were associated with IVT corridors that likely constituted a portion of the broad ascending warm conveyor belt as in Eckhardt et al. (2004).

This study used an atmospheric water vapor budget to demonstrate that decreases in IWV via precipitation processes in the presence of troposphere-deep upward vertical motion during the development phase of an AR can be subsequently offset by increases in IWV via IVT convergence and evaporation during the evolution phase of an AR. The subsequent evolution of the zonally elongated ARs in the present study occurs in association with a transition from a tropical environment to an extratropical environment characterized by QG forcing for ascent and a strong thermally direct ageostrophic circulation in the entrance region of an intensifying and zonally elongated upper-tropospheric jet streak. The extratropical environment and related dynamical processes act to sustain large IWV values in conjunction with horizontal aggregation of subtropical and extratropical water vapor along the AR corridors via frontogenesis. The dynamical processes associated with IVT convergence in the present study are similar to results documented by Bao et al. (2006) and Neiman et al. (2013), who show that some significant ARs strengthen markedly in the presence of frontogenesis and in the absence of direct water vapor transport from the tropics.

The evolution of AR_1 occurs equatorward of a frontal low that rapidly propagated across the North Pacific with characteristics similar to a diabatic Rossby wave. A diabatic Rossby wave is characterized by a lower-troposphere PV maximum that typically propagates eastward due to diabatic PV tendencies induced by latent heat release in the presence of saturated ascent along a strong lower-troposphere baroclinic zone. The environment of a zonally elongated AR, characterized by strong lower-tropospheric frontogenesis and large IWV values, may be particularly conducive to the development and rapid eastward propagation of diabatic Rossby waves. Although not discussed in the present study, Lackmann (2002) illustrates that latent heat release is an important contributor to the development and eastward propagation of elongated lower-tropospheric PV bands that accompany regions of water vapor transport in the warm sector of some cyclones. Previous studies of diabatic Rossby waves have not specifically drawn connections between zonally elongated ARs and diabatic Rossby waves; however, several studies have identified tropical moisture source regions and air parcel trajectories consistent with the warm conveyor belt region of intensifying cyclones as ingredients in at least some life cycles of diabatic Rossby waves (e.g., Wernli et al. 2002; Moore et al. 2008; Cordeira and Bosart 2011).

This study represents a noteworthy advance in the understanding of the connection between tropical processes and midlatitude ARs. Unlike Ralph et al. (2011), which used a P-3 research aircraft to document a direct "tropical tap" (i.e., tropical moisture export) in an AR event that led to heavy rain in Oregon, this study shows an indirect effect of the tropics on a midlatitude AR via dynamical processes associated with the interaction of TC and PRE-like diabatic outflow with the NPJ. The

impressive visual aspect of this event in SSM/I satellite observations and evolution of the ARs over the North Pacific belies the fact that ARs are a highly dynamic feature for which continuous regeneration of IWV through evaporation and water vapor flux convergence act to maintain the distinctive IWV signature against strong water vapor loss through precipitation.

Future work will explore the landfalling aspect of this event, including evaluation of the role of the merger of the two initially separate ARs into one strong AR at landfall. It is likely that the merging ARs contributed to both the intensity and duration of the event. These aspects will be compared with the findings of a climatological study of AR duration (Ralph et al. 2013), and of the role of the Sierra barrier jet (SBJ) in deflecting a landfalling AR upward over the SBJ (Kingsmill et al. 2013). Additionally, given that there can be significant uncertainties in the representation of key atmospheric processes in reanalysis datasets, future work is aimed at further investigations of the terms in the atmospheric water vapor budget from both a numerical modeling perspective and from aircraft and remote sensing observations. Such observations would need to recognize that the magnitudes of the precipitation rate, water vapor flux convergence, evaporation rate, and IWV tendencies vary greatly from one region to another during an event, and would need to span the complete life cycle of an AR (i.e., from the ''development'' phase to the ''evolution'' phase).

Acknowledgments. This research was conducted while the first author held a National Research Council Research Associateship Award with the Water Cycle Branch of NOAA/ESRL Physical Sciences Division. Reviews by Paul Neiman (NOAA/ESRL Physical Sciences Division), George Kiladis (NOAA/ESRL Physical Sciences Division), Thomas Galarneau, Jr. (NCAR), and Heini Wernli (Institute for Atmosphere and Climate Science, ETH) greatly improved the quality of this manuscript. The authors thank Anantha Aiyyer (North Carolina State University) for developing software to calculate air parcel trajectories and EarthRisk Technologies (San Diego, California) for computational resources and financial support during manuscript preparation.

REFERENCES

Archambault, H. M., 2011: The downstream extratropical flow response to recurving western North Pacific tropical cyclones. Ph.D. dissertation, University at Albany, State University of New York, 212 pp.

——, L. F. Bosart, D. Keyser, and J. M. Cordeira, 2013: A climatological analysis of the extratropical flow response to recurving western North Pacific tropical cyclones. *Mon. Wea. Rev.,* **141,** 2325–2346.

Atallah, E. H., and L. F. Bosart, 2003: Extratropical transition and precipitation distribution of Hurricane Floyd '99. *Mon. Wea. Rev.,* **131,** 1063–1081.

Baldwin, M. E., and K. E. Mitchell, 1997: The NCEP hourly multisensor U.S. precipitation analysis for operations and GCIP research. Preprints, *13th Conf. on Hydrology,* Long Beach, CA, Amer. Meteor. Soc., 54–55.

Bao, J.-W., S. A. Michelson, P. J. Nieman, F. M. Ralph, and J. M. Wilczak, 2006: Interpretation of enhanced integrated water vapor bands associated with extratropical cyclones: Their formation and connection to tropical moisture. *Mon. Wea. Rev.,* **134,** 1063–1080.

Bluestein, H., 1992: *Synoptic-Dynamic Meteorology in Midlatitudes.* Vol. I, *Principles of Kinematics and Dynamics.* Oxford University Press, 431 pp.

Bosart, L. F., and F. H. Carr, 1978: A case study of excessive rainfall centered around Wellsville, New York, 20–21 June 1972. *Mon. Wea. Rev.,* **106,** 348–362.

——, and D. B. Dean, 1991: The Agnes rainstorm of June 1972: Surface feature evolution culminating in inland storm redevelopment. *Wea. Forecasting,* **6,** 515–537.

——, J. M. Cordeira, T. J. Galarneau Jr., B. J. Moore, and H. M. Archambault, 2012: Predecessor rain events associated with tropical cyclones Ike and Lowell (11 to 14 September 2008). *Mon. Wea. Rev.,* **140,** 1081–1107.

Browning, K. A., 1990: Organization of clouds and precipitation in extratropical cyclones. *Extratropical Cyclones: The Erik Palmén Memorial Volume,* C. W. Newton and E. Holopainen, Eds., Amer. Meteor. Soc., 129–153.

Byun, K.-Y., and T.-Y. Lee, 2012: Remote effects of tropical cyclones on heavy rainfall over the Korean peninsula—Statistical and composite analysis. *Tellus,* **64,** 14983, doi:10.3402/tellusa.v64i0.14983.

Carlson, T. N., 1980: Airflow through midlatitude cyclones and the comma cloud pattern. *Mon. Wea. Rev.,* **108,** 1498–1509.

——, 1998: *Mid-Latitude Weather Systems.* Amer. Meteor. Soc., 507 pp.

Cordeira, J. M., and L. F. Bosart, 2011: Cyclone interactions and evolutions during the ''Perfect Storms'' of late October and early November 1991. *Mon. Wea. Rev.,* **139,** 1683–1707.

Cote, M. R., 2007: Predecessor rain events in advance of tropical cyclones. M.S. thesis, Department of Atmospheric and Environmental Sciences, University at Albany, State University of New York, 200 pp. [Available online at http://cstar.cestm.albany.edu/CAP_Projects/Project10/index.htm.]

Davies, H. C., and A. M. Rossa, 1998: PV frontogenesis and upper-tropospheric fronts. *Mon. Wea. Rev.,* **126,** 1528–1539.

Eckhardt, S., A. Stohl, H. Wernli, P. James, C. Forster, and N. Spichtinger, 2004: A 15-year climatology of warm conveyor belts. *J. Climate,* **17,** 218–237.

Galarneau, T. J., L. F. Bosart, and R. S. Schumacher, 2010: Predecessor rain events ahead of tropical cyclones. *Mon. Wea. Rev.,* **138,** 3272–3297.

Grams, C. M., S. C. Jones, C. A. Davis, P. A. Harr, and M. Weissmann, 2013: The impact of Typhoon Jangmi (2008) on the midlatitude flow. Part I: Upper-level ridgebuilding and modification of the jet. *Quart. J. Roy. Meteor. Soc.,* doi:10.1002/qj.2091, in press.

Harr, P. A., and R. L. Elsberry, 2000: Extratropical transition of tropical cyclones over the western North Pacific. Part I: Evolution of structural characteristics during the transition process. *Mon. Wea. Rev.,* **128,** 2613–2633.

——, and J. M. Dea, 2009: Downstream development associated with the extratropical transition of tropical cyclones over the western North Pacific. *Mon. Wea. Rev.,* **137,** 1295–1319.

Hollinger, J. P., Ed., 1991: Defense meteorological satellite program special sensor microwave/imager calibration/validation. Vol. II. Naval Research Laboratory Tech. Rep., 304 pp.

Hoskins, B. J., I. Draghici, and H. C. Davies, 1978: A new look at the omega equation. *Quart. J. Roy. Meteor. Soc.,* **104,** 31–38.

Huffman, G. J., and Coauthors, 2007: The TRMM Multisatellite Precipitation Analysis (TMPA): Quasi-global, multiyear, combined-sensor precipitation estimates at fine scales. *J. Hydrometeor.,* **8,** 38–55.

Keyser, D., M. J. Reeder, and R. J. Reed, 1988: A generalization of Petterssen's frontogenesis function and its relation to the forcing of vertical motion. *Mon. Wea. Rev.,* **116,** 762–781.

Kingsmill, D. E., P. J. Neiman, B. J. Moore, M. Hughes, S. E. Yuter, and F. M. Ralph, 2013: Kinematic and thermodynamic structures of Sierra barrier jets and overrunning atmospheric rivers during a landfalling winter storm in northern California. *Mon. Wea. Rev.,* **141,** 2015–2036.

Klein, P. M., P. A. Harr, and R. L. Elsberry, 2002: Extratropical transition of western North Pacific tropical cyclones: Midlatitude and tropical cyclone contributions to reintensification. *Mon. Wea. Rev.,* **130,** 2240–2259.

Knippertz, P., 2007: Tropical-extratropical interactions related to upper-level troughs at low latitudes. *Dyn. Atmos. Oceans,* **43,** 36–62.

——, and J. E. Martin, 2007: A Pacific moisture conveyor belt and its relationship to a significant precipitation event in the semiarid southwestern United States. *Wea. Forecasting,* **22,** 125–144.

——, and H. Wernli, 2010: A Lagrangian climatology of tropical moisture exports to the Northern Hemispheric extratropics. *J. Climate,* **23,** 987–1003.

——, ——, and G. Gläser, 2013: A global climatology of tropical moisture exports. *J. Climate,* **26,** 3031–3045.

Koch, S. E., M. desJardins, and P. J. Kocin, 1983: An interactive Barnes objective map analysis scheme for use with satellite and conventional data. *J. Climate Appl. Meteor.,* **22,** 1487–1503.

Lackmann, G. M., 2002: Cold-frontal potential vorticity maxima, the low-level jet, and moisture transport in extratropical cyclones. *Mon. Wea. Rev.,* **130,** 59–74.

McGuirk, J. P., A. H. Thompson, and N. R. Smith, 1987: Moisture bursts over the tropical Pacific Ocean. *Mon. Wea. Rev.,* **115,** 787–798.

McTaggart-Cowan, R., L. F. Bosart, J. R. Gyakum, and E. H. Atallah, 2007a: Hurricane Katrina (2005). Part I: Complex life cycle of an intense tropical cyclone. *Mon. Wea. Rev.,* **135,** 3905–3926.

——, ——, ——, and ——, 2007b: Hurricane Katrina (2005). Part II: Evolution and hemispheric impacts of a diabatically generated warm pool. *Mon. Wea. Rev.,* **135,** 3927–3949.

Miller, J. E., 1948: On the concept of frontogenesis. *J. Meteor.,* **5,** 169–171.

Moore, B. J., 2010: Synoptic-scale environments and dynamical mechanisms associated with predecessor rain events ahead of tropical cyclones. M.S. thesis, Department of Atmospheric and Environmental Sciences, University at Albany, State University of New York, 150 pp.

——, P. J. Neiman, F. M. Ralph, and F. E. Barthold, 2012: Physical processes associated with heavy flooding rainfall in Nashville, Tennessee, and vicinity during 1–2 May 2010: The role of an atmospheric river and mesoscale convective systems. *Mon. Wea. Rev.,* **140,** 358–378.

——, L. F. Bosart, D. Keyser, and M. L. Jurewicz, 2013: Synoptic-scale environments of predecessor rain events occurring east of the Rocky Mountains in association with Atlantic basin tropical cyclones. *Mon. Wea. Rev.,* **141,** 1022–1047.

Moore, R. W., M. T. Montgomery, and H. C. Davies, 2008: The integral role of a diabatic Rossby vortex in a heavy snowfall event. *Mon. Wea. Rev.,* **136,** 1878–1897.

Neiman, P. J., F. M. Ralph, G. A. Wick, Y.-H. Kuo, T.-K. Wee, Z. Ma, G. H. Taylor, and M. D. Dettinger, 2008a: Diagnosis of an intense atmospheric river impacting the Pacific Northwest: Storm summary and offshore vertical structure observed with COSMIC satellite retrievals. *Mon. Wea. Rev.,* **136,** 4398–4420.

——, ——, ——, J. D. Lundquist, and M. D. Dettinger, 2008b: Meteorological characteristics and overland precipitation impacts of atmospheric rivers affecting the west coast of North America based on eight years of SSM/I satellite observations. *J. Hydrometeor.,* **9,** 22–47.

——, L. J. Schick, F. M. Ralph, M. Hughes, and G. A. Wick, 2011: Flooding in western Washington: The connection to atmospheric rivers. *J. Hydrometeor.,* **12,** 1337–1358.

——, F. M. Ralph, B. J. Moore, M. Hughes, K. Mahoney, J. M. Cordeira, and M. D. Dettinger, 2013: The landfall and inland penetration of a flood-producing atmospheric river in Arizona. Part I: Observed synoptic-scale, orographic, and hydrometeorological characteristics. *J. Hydrometeor.,* **14,** 460–484.

Ralph, F. M., and M. D. Dettinger, 2011: Storms, floods and the science of atmospheric rivers. *Eos, Trans. Amer. Geophys. Union,* **92,** 265–266.

——, and ——, 2012: Historical and national perspectives on extreme West Coast precipitation associated with atmospheric rivers during December 2010. *Bull. Amer. Meteor. Soc.,* **93,** 783–790.

——, P. J. Neiman, D. E. Kingsmill, P. O. G. Persson, A. B. White, E. T. Strem, E. D. Andrews, and R. C. Antweiler, 2003: The impact of a prominent rain shadow on flooding in California's Santa Cruz Mountains: A CALJET case study and sensitivity to the ENSO cycle. *J. Hydrometeor.,* **4,** 1243–1264.

——, ——, and G. A. Wick, 2004: Satellite and CALJET aircraft observations of atmospheric rivers of the eastern North Pacific Ocean during the winter of 1997/98. *Mon. Wea. Rev.,* **132,** 1721–1745.

——, ——, and R. Rotunno, 2005: Dropsonde observations in low-level jets over the northeastern Pacific Ocean from CALJET-1998 and PACJET-2001: Mean vertical-profile and atmospheric-river characteristics. *Mon. Wea. Rev.,* **133,** 889–910.

——, ——, G. A. Wick, S. I. Gutman, M. D. Dettinger, D. R. Cayan, and A. B. White, 2006: Flooding on California's Russian River: Role of atmospheric rivers. *Geophys. Res. Lett.,* **33,** L13801, doi:10.1029/2006GL026689.

——, ——, G. N. Kiladis, K. Weickmann, and D. W. Reynolds, 2011: A multiscale observational case study of a Pacific atmospheric river exhibiting tropical–extratropical connections and a mesoscale frontal wave. *Mon. Wea. Rev.,* **139,** 1169–1189.

——, T. Coleman, P. J. Neiman, R. J. Zamora, and M. D. Dettinger, 2013: Observed impacts of duration and seasonality of atmospheric-river landfalls on soil moisture and runoff in coastal Northern California. *J. Hydrometeor.,* **14,** 443–459.

Riemann-Campe, K., K. Fraedrich, and F. Lunkeit, 2009: Global climatology of convective available potential energy (CAPE) and convective inhibition (CIN) in ERA-40 reanalysis. *Atmos. Res.,* **93,** 534–545.

Riemer, M., and S. C. Jones, 2010: The downstream impact of tropical cyclones on a developing baroclinic wave in idealized scenarios of extratropical transition. *Quart. J. Roy. Meteor. Soc.,* **136,** 617–637.

——, ——, and C. A. Davis, 2008: The impact of extratropical transition on the downstream flow: An idealized modeling study with a straight jet. *Quart. J. Roy. Meteor. Soc.,* **134,** 69–91.

Saha, S., and Coauthors, 2010: The NCEP Climate Forecast System Reanalysis. *Bull. Amer. Meteor. Soc.,* **91,** 1015–1057.

Schmitz, T. J., and S. L. Mullen, 1996: Water vapor transport associated with the summertime North American monsoon as depicted by ECMWF analyses. *J. Climate,* **9,** 1621–1633.

Schumacher, R. S., T. J. Galarneau Jr., and L. F. Bosart, 2011: Distant effects of a recurving tropical cyclone on rainfall in a midlatitude convective system: A high-impact predecessor rain event. *Mon. Wea. Rev.,* **139,** 650–667.

Shapiro, M. A., 1982: Mesoscale weather systems of the central United States. University of Colorado, Boulder, CO, Cooperative Institute for Research in Environmental Sciences (CIRES)/National Oceanographic and Atmospheric Administration (NOAA), 78 pp.

Smith, B. L., S. E. Yuter, P. J. Neiman, and D. E. Kingsmill, 2010: Water vapor fluxes and orographic precipitation over northern California associated with a landfalling atmospheric river. *Mon. Wea. Rev.,* **138,** 74–100.

Stohl, A., and P. James, 2004: A Lagrangian analysis of the atmospheric branch of the global water cycle. Part I: Method description, validation, and demonstration for the August 2002 flooding in central Europe. *J. Hydrometeor.,* **5,** 656–678.

——, C. Forster, and H. Sodemann, 2008: Remote sources of water vapor forming precipitation on the Norwegian west coast at 60°N—A tale of hurricanes and an atmospheric river. *J. Geophys. Res.,* **113,** D05102, doi:10.1029/2007JD009006.

Trenberth, K. E., and C. J. Guillemot, 1996: Physical processes involved in the 1988 drought and 1993 floods in North America. *J. Climate,* **9,** 1288–1298.

Wang, Y., Y. Wang, and H. Fudeyasu, 2009: The role of Typhoon Songda (2004) in producing distantly located heavy rainfall in Japan. *Mon. Wea. Rev.,* **137,** 3699–3716.

Waugh, D. W., and B. M. Funatsu, 2003: Intrusions into the tropical upper troposphere: Three-dimensional structure and accompanying ozone and OLR distributions. *J. Atmos. Sci.,* **60,** 637–653.

Wernli, H., S. Dirren, M. A. Liniger, and M. Zillig, 2002: Dynamical aspects of the life cycle of the winter storm 'Lothar' (24–26 December 1999). *Quart. J. Roy. Meteor. Soc.,* **128,** 405–429.

Zhu, Y., and R. E. Newell, 1998: A proposed algorithm for moisture fluxes from atmospheric rivers. *Mon. Wea. Rev.,* **126,** 725–735.